Investigating Electron Optical Properties of Large Aperture Quadrupoles for MESA

Author:
Nahid Scahill

Supervisor:
Professor Dr. Kurt Aulenbacher

THESIS

Submitted in partial fulfilment of the requirements
for the degree of Master of Science in Physics
in the Fachbereich 08 at
Johannes Gutenberg-Universität Mainz

JOHANNES GUTENBERG
UNIVERSITÄT MAINZ

May 2015

To my dear sons,
Michael, Daniel, Andrew, and Joshua

"Shoot for the moon.
Even if you miss,
you'll land among the stars."

-Norman Vincent Peale

Declaration Of Authorship

> “I do solemnly declare that I have written the presented research thesis by myself without undue help from a second person others and without using such tools other than that specified. Where I have used thoughts from external sources, directly or indirectly, published or unpublished, this is always clearly attributed.
> Furthermore, I certify that this research thesis or any part of it has not been previously submitted for a degree or any other qualification at the Johannes Gutenberg-Universität Mainz or any other institution in Germany or abroad.”

Nahid Scahill
May 15th, 2015

Nahid Scahill
Institute for Kernphysik
Johann- Joachim-Becher-Weg 45
Johannes Gutenberg- Universitat D-55099 Mainz
nscahill@uni-mainz.de

Contents

1. Introduction **6**
1.1. Motivation of the Research 6
1.2. Contents of the Thesis 10

2. Theory **12**
2.1. Trajectory Equation of an Electron through the Magnetic Field . . . 12
2.2. Linear Beam Transport System 12
2.3. Matrix Formalism in Linear Beam Optics 13
2.3.1. Drift Space 15
2.3.2. Quadrupole Magnet 15
2.4. Quadrupole End-Field Effect 17
2.5. The Quadrupole Doublet 22
2.6. The Phase Space Ellipse and the Twiss Parameters 23
2.7. The Electron Optical Properties of the Wien Filter 24

3. Research Approach and Experiment I **27**
3.1. Large Aperture Quadrupoles 27
3.2. Hard-Edge Quadrupole 30
3.2.1. Reference Quadrupole 31
3.2.2. Measuring the Magnetic Field of the Reference Quadrupole and the Quadrupoles in the PKAT 33
3.2.3. Measuring the Magnetic Field Gradient of the Reference Quadrupole 35
3.3. Finding the Focused Beam Size Using the Magnetic Field Gradient . 37

4. Research Approach and Experiment II **40**
4.1. Transformation Matrix by Dividing the Quadrupole into Small Sections 40
4.1.1. Finding the Quadrupole Overall Transformation Matrix . . . 40
4.1.2. Investigating the Stability of the Transformation Matrix Elements 41
4.1.3. Finding the Best Focused Beam Size Using the Overall Transformation Matrix 44
4.2. Comparing the Theoretical and Experimental Values 45
4.3. True Quadrupole Effective Parameters 45
4.4. Correction due to the Extended Gradient 50

5. Quadrupole Doublet **53**
5.1. Hard-Edge Model 54
5.1.1. Horizontal and Vertical Planes 54
5.1.2. Both Planes 56
5.2. Overall Transformation Matrix 56
5.2.1. Horizontal and Vertical Planes 58
5.2.2. Both Planes 59
5.3. Comparing the Theoretical and Experimental Values 59

6. Conclusion **63**

7. Outlook **64**

A. Tables of Data **69**
A.1. Single Quadrupole, Hard-Edge 69
A.2. Single Quadrupole, Overall Transformation Matrix 70
B.1. Field Fringe Deviations 71
C.1. Quadrupole Doublet, Hard-Edge 72
D.1. Quadrupole Doublet, Overall Transformation Matrix 73
D.1.1. Horizontal and Vertical Plane 73

1. Introduction

1.1. Motivation of the Research

Nowadays scattering experiments with spin-polarized electron beams are in the forefront of fundamental researches in nuclear physics. They play an important role in understanding the behaviour of the matter. It is through such experiments that is possible to, for example, investigate the electroweak mixing angle and measure the weak charge of the proton, which can be achieved by measuring the parity-violating asymmetry [1] in elastic electron-proton scattering at low momentum transfer. Performing these high precision experiments successfully requires very highly polarized beams and demands optimum properties of the accelerator. 000 One such accelerator, which is currently under construction, is the Mainz Energy Recovering Superconducting Accelerator, MESA, located at the Institute for nuclear physics, IKPH, at Johannes Gutenberg University of Mainz. The operation of MESA will be independent of the currently existing accelerator, Mainzer Mikroton, MAMI. MESA, which is scheduled to be in operation by the end of 2017 [2][2], is being constructed in the limited available footprint area of approximately 7.7 m × 27 m [3]. In Fig. 1.1 a sketch of the new accelerator, MESA, is demonstrated.

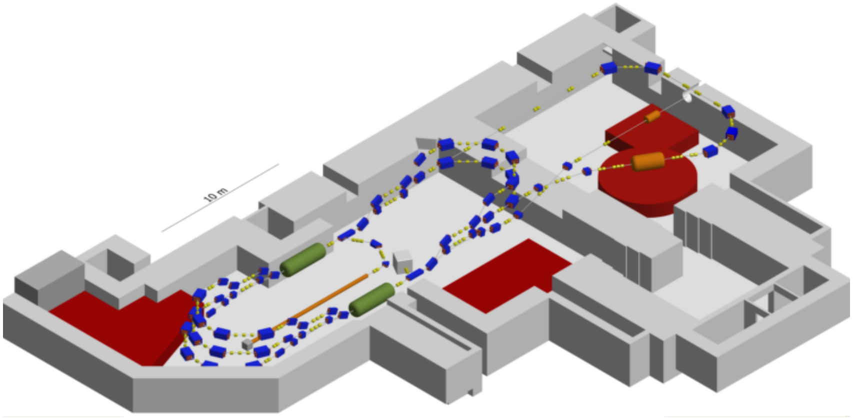

Figure 1.1.: Sketch of MESA, the new accelerator under construction in Mainz. In the layout, the blue elements represent dipoles. The quadrupoles, which are located in between the dipoles are shown in yellow.

This multi-turn energy recovery linac is designed to offer unique opportunities for several experiments in particle and hadron physics and especially parity violating electron scattering [4]. Due to the restrictions in space and budget, the concept of a multi-turn acceleration is necessary [4]. MESA is intended to accommodate particle physics experiments in the 100 MeV – 200 MeV energy range [5]. MESA, which will be an extension [6] to the experimental facilities already existing in IKPH, MAMI, will complement the experimental possibilities of MAMI and therefore, a wider parameter range [5] could be investigated at the IKPH.

For an efficient design [5], construction of MESA is relying on employing superconducting technology for the main linac, which allows providing an energy gain of 50 MeV per turn [2]. This multi-turn recirculating linac will be operated [3] in 2 modes: an energy recovery, (ER), mode which is designed to accelerate unpolarized electrons to a high current up to 10 mA at 105 MeV to sustain the 1 MW of beam power [5], and an external beam, (EB), mode for the low intensity polarized electron beam which accelerates them to a maximum energy of 155 MeV at a current of 150 µA.

The MESA injector will be equipped with a 100 keV photo source followed by a chopper and a harmonic buncher [6]. All components of the injector will basically be copies of MAMI accelerating systems, which has the well proven design for many years [5]. The easier spin measurement and manipulation at lower energy are the reason for the 100 keV restriction [5]. In the MESA accelerating system, as in MAMI operation, GaAs/ GaAsP superlattice photocathodes [7] will provide highly polarized beam ($P \approx 0.85$) [6].

The MESA accelerator is designed with the first priority of supplying beam for particle and nuclear physics experiments [4] and a primary goal of providing optimum operation conditions for the parity violating experiments in particular [4,6] . The parity violating electron scattering experiments, which for many years [6] have been carried out by the c.w. electron accelerator MAMI, now are planned to be accomplished by the MESA.

In particular, the MESA accelerator is designed to perform two experiments [5]:

1. Precision measurement of the Weinberg angle, which will be achieved in the EB mode

2. The search for dark photons [8], which will be performed in the ER mode

The high precision parity violating experiments, called P2, which aim at determining the weak charge of the proton [1], demand a low beam energy of 150 MeV [6], and require a very good control of the beam parameters [4], which, therefore, necessitate the condition of having very high stability of the accelerator.

MESA will provide approximately 4000 h of beam time per year [1] for the P2 experiment alone. The project P2 measurement requires a longitudinally highly polarized beam of electrons which will be detected after being elastically scattered [1] from protons in a liquid-hydrogen target. Achieving an accuracy in the beam polarization measurement is one of the main challenges of the parity violating electron scattering [6]. The polarization accuracy must be below the attempted accuracy in the determination of $\sin^2(\theta_\omega)$, which means less than 0.3 % [6].

Some of the limitations of polarization degree and accelerator performance are due to the physics of photoemission in the semiconductor cathodes that are employed. The time resolved polarization experiments are not only useful for the P2 measurements, but interesting semiconductor physics by itself as well. Today, most time resolved measurements employ short optical laser pulses on the femtosecond time-scale in order to excite electrons from the valence to the conduction band of the semiconductor. This excitation initializes the spin orientation. Consequently, the time resolved polarization experiment measures the temporal evolution of the degree of the polarization [9].

The time resolved measurements provide means of gaining knowledge in identifying the depolarization process in the cathode. Through the time resolved measurements, one could, for instance, observe the response time and spin relaxation time of thin unstrained and strained III/V semiconductor photocathodes installed in sources of polarized electrons [10]. Also, experimental studies of spin polarized electron transport in strained semiconductor superlattice used for photoemitter application could be performed [11].

The long-term objective of this specific research, which is planned to be accomplished following the completion of the investigation of the electron optical properties of the large aperture quadrupoles, is to perform the time resolved polarization measurements and obtain the spin polarization and relaxation time.

Having a good knowledge of the spin relaxation time of the photecathode will create opportunities for higher polarization. Since the measurement time in the polarization experiments is proportional to the inverse of the polarization squared, $T_{\text{mearurement}} \propto \frac{1}{P^2}$, achieving for example a 10 % increase in the spin polarization will result in almost 20 % less measurement time. In the case of the MESA accelerator, this means 800 h less beam time per year for the polarization measurements, which is very significant.

The source of polarized electrons is based on photoelectron emission of semiconductor crystals. The strained layer superlattice photocathodes are currently known to be the most effective way of producing highly polarized electrons [11] . The electrons are emitted from a strained layer semiconductor superlattice photocathode, such as GaAs/GaAsP, after its photoexcitation by a femtosecond laser pulse [12].

These polarized sources produce longitudinally polarized electrons, which means the spin polarization vector is oriented along the particles' momentum. However, the polarization of the low energy electrons is usually measured by a Mott polarimeter which requires the polarization to be transverse to the scattering plane. Therefore, performing the time resolved polarization measurements demands the spin of the electrons to be rotated before the experiment. This necessitates the use of a spin rotation system such as a Wien filter [13], in order to rotate the initially longitudinal polarization of the beam and transform it into a transverse polarization.

A Wien filter allows the spin of the particle to be rotated to the desired orientation for different energies without affecting the emittance or the energy of the electrons.

However, since the Wien filter has a very strong quadrupole component in one direction, one must obtain good quadrupole focusing to be able to compensate for that. The details of the design and the functionality of the Wien filter will be discussed more thoroughly in the following chapter.

One of the major factors to achieve a successful operation of an accelerator is having detailed knowledge of the functionality of the components used in the beam line system. Having a comprehensive understanding of the components' functionality allows proper prediction of charged particle beam behaviour in the accelerator which in turn, results in the design of the accelerator meeting specific goals.

The quadrupoles are the most basic building blocks in the design of any modern particle accelerator. For example, the new accelerator in Mainz, MESA, will be constructed with more than 130 quadrupoles, a number much higher than of any other elements in the accelerator beam line. Therefore, in general it is of particular importance to study the behaviour of the quadrupoles in depth. In our specific research this is significant because of the two-fold following reasons:

- Both the quadrupoles that will be needed for the operation of MESA, which are located right after the source injector system and the ones which are currently being used in the injection system of MAMI, called the Polarisierte Kanone Test, PKAT in short, have a high ratio of aperture to length. This means the distance between the opposite pole faces is large as compared to the length of the pole faces. The ratio of the aperture to the length in these quadrupoles is almost equal to 1. Having large aperture quadrupole will result in the customary definitions of the quadrupole effective strength and length not being accurate in reality.

- Prepration for the time resolved spin polarization measurements in the PKAT beam transport system necessitates the use of a Wien filter to rotate the spin polarization of the electrons, which subsequently requires having a good quadrupole focusing.

Therefore, in order to achieve and maintain the reliability of the operation and performance of MESA, and successfully reach the optimum goals for which MESA is designed and furthermore, be able to successfully perform the time resolved polarization measurements and obtain higher polarization it is essential to specially study the behaviour of the large aperture quadrupoles. It is for this specific purpose that this research has been performed.

To better understand the behaviour of the large aperture quadrupoles in the beam line, our main focus has been investigating the exact quadrupole parameters necessary to insert in the Beam Optic computer simulation program. By using the Beam Optic simulation program, one could visually construct any accelerator system graphically, and examine the properties of the selected beam line system in a short time. Beam Optic is designed to compute transport matrices, beam envelopes, beam size, and trajectories.

In order to achieve the goal of studying the behaviour of these large aperture quadrupoles, our primary focus has been to determine which current will produce the most focused beam through these quadrupoles.

The motivation for this research arose from the large discrepancy of the value of the current, and therefore the focal length, needed to obtain the minimum beam size between the theoretical value when the quadrupole is treated as a hard-edge quadrupole with an effective length l_{eff}, and the experimental value. This discrepancy has been almost c. As a result, a modification to the conventional beam transport is required, and depending on the excitation of such quadrupoles a correction to the quadrupole strength and effective length must be made.

1.2. Contents of the Thesis

The steps that are taken to accomplish the task of this research, which is to investigate the electron optical properties of the large aperture quadrupoles for MESA, and obtain more accurate quadrupole parameters, are as follows:

After introducing some theoretical concepts of the motion of the electrons in a beam transport system and explaining the matrix formulation, the quadrupole end effect is described. Then, the quadrupole doublet and the matrix formulation associated with the doublet are discussed. The Twiss parameters are introduced and finally the electron optical properties of the Wien filter are explained briefly. These materials are assembled in Chapter 2.

The research presented in this thesis, which consists of using two different approaches, is divided into three chapters:

- The first part of the research uses the approach of a hard-edge model for quadrupoles and consists of selecting a quadrupole reference, to measure the field gradient in place of the quadrupoles built into the present beam line structure of the PKAT. Then, by applying the Beam Optic simulation program and using the magnetic field gradient of the hard-edge model for the quadrupole, the current to obtain the most focused beam from the first quadrupole in the PKAT beam transport system is determined. This approach is presented in Chapter 3.

- In Chapter 4, the second part of our approach, which considers the matrix formulation and the improved treatment of the quadrupole end effect, is described. In this chapter, the transformation matrix has been calculated by dividing the quadrupole into 800 small hard-edge quadrupoles and combining their respective matrices. These matrix parameters are used in the Beam Optic computer simulation program to find the current to achieve the most focused beam. Then, at the end, the deviations and, therefore, the necessary corrections to the customary definition of the quadrupole effective length and strength are calculated. Again, in this chapter, for the simplicity, the simulation is performed based on considering only the first quadrupole in the PKAT transport system.

- Finally, in the last part of the research, the first quadrupole doublet in the PKAT beam line is studied. The approaches from the two previous chapters, i.e. the hard-edge model and the overall transformation matrix technique, are applied to the quadrupole doublet. Again, by using the Beam Optic simulation program, the current to achieve the focused beam for this doublet is determined and compared with the experimental value. The treatment for the quadrupole doublet is explained in Chapter 5.

The results and the conclusion of this project are discussed in Chapter 6, followed by the applications and suggestions how to implement the results of this research in the operation of the accelerator, and in preparation for the performance of the time resolved polarization measurements, along with some suggestions on how to expand this research further in the future. These materials are put together in Chapter 7.

2. Theory

2.1. Trajectory Equation of an Electron through the Magnetic Field

Particle accelerators and beam transport systems provide a beam guidance and focusing system. A beam of charged particles is expected to follow closely a predefined path along a desired beam transport line. The forces required to bend, steer, and focus are known as the Lorentz forces. The Lorentz force for an electron with velocity $\boldsymbol{v}$ passing through a volume containing a magnetic field $\boldsymbol{B}$ and an electric field $\boldsymbol{E}$ is expressed by

$$\frac{\mathrm{d}}{\mathrm{d}t}(m\boldsymbol{v}) = e(\boldsymbol{E} + \boldsymbol{v} \times \boldsymbol{B}) \tag{2.1}$$

with m being the mass of the electron.

2.2. Linear Beam Transport System

Since it is much easier to produce a magnetic field than an electric field of the equivalent effect, magnets are mainly used to steer the beam in standard high energy beam handling practices. One can achieve the basic goals of beam dynamics by using only two types of magnets, bending magnets (dipoles) and quadrupoles. The theory of particle dynamics in the presence of only such magnets is referred to as linear beam optics [14].

Consider the motion of an electron near the ideal trajectory direction z. Let us assume a Cartesian coordinate system (x, y, z), whose origin moves along the trajectory of the beam. Furthermore, assume that the electrons move parallel to the ideal trajectory direction z and also that the magnetic field only has transverse components, which means it has the form $\boldsymbol{B} = (B_x, B_y, 0)$.

For an electron moving through the magnetic field in the horizontal plane, by balancing the Lorentz force and the centrifugal force, one will obtain

$$\frac{1}{R(x)} = \frac{e}{p}B_y(x) \tag{2.2}$$

where R is the radius of the curvature of the trajectory and p is the momentum of the electron. There is a similar expression for the vertical plane. Expanding the magnetic field in the vicinity of the ideal trajectory of z, since the transverse

Table 2.1.: The most important multipoles with their specific effects [14]

multipole	definition	effect
dipole	$\frac{1}{R} = \frac{e}{p}B_{y0}$	beam steering
quadrupole	$k = \frac{e}{p}\frac{\mathrm{d}B_y}{\mathrm{d}x}$	beam focusing
sextupole	$m = \frac{e}{p}\frac{\mathrm{d}^2B_y}{\mathrm{d}x^2}$	chromaticity compensation
octupole	$o = \frac{e}{p}\frac{\mathrm{d}^3B_y}{\mathrm{d}x^3}$	field errors or field compensation

dimensions of the electron ensembles are much smaller than the radius of curvature, and then multiplying by $\frac{e}{p}$, we will obtain

$$\begin{aligned}\frac{e}{p}B_y(x) &= \frac{e}{p}B_{y0} + \frac{e}{p}\frac{dB_y}{dx}x + \frac{1}{2!}\frac{e}{p}\frac{d^2B_y}{dx^2}x^2 + \frac{1}{3!}\frac{e}{p}\frac{d^3B_y}{dx^3}x^3 + \ldots\\ &= \underbrace{\frac{1}{R}}_{\text{dipole}} + \underbrace{kx}_{\text{quadrupole}} + \underbrace{\frac{1}{2!}mx^2}_{\text{sextupole}} + \underbrace{\frac{1}{3!}ox^3}_{\text{octupole}} + \ldots\end{aligned}$$

which is to say the effect of the magnetic field on the beam is in fact the sum of the different multipoles. Table 2.1 presents the most important multipoles with their specific effects.

Each of these multipoles has a unique effect on the motion of the charged particles as they go through the beam line. For example, while the first term in the equation, dipole, is mainly responsible for steering the beam, the result of the second term, quadrupole, is to focus the beam.

2.3. Matrix Formalism in Linear Beam Optics

The linear equation of motion for an electron travelling through a magnetic field in the vicinity of the ideal trajectory, in the system described above, with the assumptions that the electrons have a well-defined momentum, and that they are deflected only in the horizontal plane could be written as [14]

$$\frac{\mathrm{d}^2X(z)}{\mathrm{d}z^2} + k(z)X(z) = 0 \tag{2.3}$$

This homogeneous and linear second-order differential equation has the form of a harmonic oscillator equation. In solving this equation, we further assume that the magnetic field begin and end abruptly at the beginning and the end of the magnet. In addition, we assume that the magnetic field is constant along the beam axis. This rectangular shape assumption of the magnetic field is known as the hard-edge model [14].

Now, we consider two cases depending on the sign of the magnetic strength k. In the case of a horizontally focusing magnet with $k > 0$, the solutions of this differential equation are

$$C(z) = \cos(\sqrt{k}z) \qquad \text{and} \qquad S(z) = \frac{1}{\sqrt{k}} \sin(\sqrt{k}z) \tag{2.4}$$

and for a defocusing magnet with $k < 0$ we obtain

$$C(z) = \cosh(\sqrt{|k|}z) \qquad \text{and} \qquad S(z) = \frac{1}{\sqrt{|k|}} \sinh(\sqrt{|k|}z) \tag{2.5}$$

Note that these linearly independent solutions satisfy the following initial conditions

$$C(0) = 1 \qquad \text{and} \qquad C'(0) = \frac{dC}{dz} = 0 \tag{2.6}$$

$$S(0) = 0 \qquad \qquad S'(0) = \frac{dS}{dz} = 1 \tag{2.7}$$

In a general form, any arbitrary solution can be expressed as a linear combination of these two solutions:

$$u(z) = C(z)u_0 \ + S(z)u'_0 \tag{2.8}$$

$$u'(z) = C'(z)u_0 + S'(z)u'_0 \tag{2.9}$$

where u_0 and u'_0 are arbitrary initial parameters for the particle trajectory and the derivatives are taken with respect to z, the independent variable.

These equations, which describe the evolution of the trajectory vector within the magnet, may be expressed in matrix form:

$$\begin{pmatrix} u(z) \\ u'(z) \end{pmatrix} = \begin{pmatrix} C_u(z) & S_u(z) \\ C'_u(z) & S'_u(z) \end{pmatrix} \begin{pmatrix} u_0 \\ u'_0 \end{pmatrix} \tag{2.10}$$

where u may be used for either x or y. We can separate the motion in planes since in the linear approximation the horizontal and vertical component of the particle motion are independent of each other. In other words, there is no coupling between the x and y planes.

These solutions can be applied to any arbitrary beam transport line as long as we assume the focusing parameter k within each individual element of the beam line is constant and that it changes in a step-like function along the beam transport line [15].

Now, we will discuss the linear (2×2) transformation matrices for drift space and quadrupole magnet.

2.3.1. Drift Space

For a drift space of length l, the focusing parameter $k = 0$, and therefore the solution of the equation of motion could be expressed as

$$\begin{pmatrix} u(z) \\ u'(z) \end{pmatrix} = \begin{pmatrix} 1 & l \\ 0 & 1 \end{pmatrix} \begin{pmatrix} u_0 \\ u'_0 \end{pmatrix} \tag{2.11}$$

As we expected for a particle travelling through a field free drift space, the amplitude u changes from the initial amplitude of u_0 by lu'_0 , assuming that $u'_0 \neq 0$, while the slope itself, u', remains constant. Therefore any drift space of length $l = z - z_0$ in the matrix formalism is represented simply by the transformation matrix

$$M_d(l|0) = \begin{pmatrix} 1 & l \\ 0 & 1 \end{pmatrix} \tag{2.12}$$

2.3.2. Quadrupole Magnet

Consider a perfect, pure quadrupole with an effective length l and constant magnetic field focusing strength k_0, which could be positive or negative depending on whether the quadrupole is focusing or defocusing.

For a focusing quadrupole, $k_0 > 0$, after solving the equation of motion, equation (2.3), and choosing the initial conditions, one will obtain the linear transformation of the quadrupole

$$\begin{pmatrix} u(z) \\ u'(z) \end{pmatrix} = \begin{pmatrix} \cos\varphi & \frac{1}{\sqrt{k_0}}\sin\varphi \\ -\sqrt{k_0}\sin\varphi & \cos\varphi \end{pmatrix} \begin{pmatrix} u(z_0) \\ u'(z_0) \end{pmatrix} \tag{2.13}$$

where $\varphi = l\sqrt{k_0}$. Therefore the transformation matrix for a focusing quadrupole is

$$M_{QF}(l|0) = \begin{pmatrix} \cos\varphi & \frac{1}{\sqrt{k_0}}\sin\varphi \\ -\sqrt{k_0}\sin\varphi & \cos\varphi \end{pmatrix} \tag{2.14}$$

The matrix element M_{21} could be identified with the inverse of the focal length of a thin lens in the geometrical light optics. This means

$$\frac{1}{f} = -\sqrt{k_0}\sin\varphi \tag{2.15}$$

Similarly, for the defocusing quadrupole, $k_0 < 0$, under the same conditions, and choosing $\varphi = l\sqrt{|k_0|}$ the transformation matrix will be

$$\begin{pmatrix} u(z) \\ u'(z) \end{pmatrix} = \begin{pmatrix} \cosh\varphi & \frac{1}{\sqrt{|k_0|}}\sinh\varphi \\ \sqrt{|k_0|}\sinh\varphi & \cosh\varphi \end{pmatrix} \begin{pmatrix} u(z_0) \\ u'(z_0) \end{pmatrix} \tag{2.16}$$

which means the transformation matrix for a defocusing quadrupole could be written as

$$M_{QD}(l|0) = \begin{pmatrix} \cosh\varphi & \frac{1}{\sqrt{|k_0|}}\sinh\varphi \\ \sqrt{|k_0|}\sinh\varphi & \cosh\varphi \end{pmatrix} \tag{2.17}$$

and again the M_{21} element determines the inverse of the focal length of a defocusing quadrupole, which means

$$\frac{1}{f} = \sqrt{|k_0|}\sinh\varphi \tag{2.18}$$

If we wish to consider the general motion of the particle in both planes, (x, z) and (y, z), as the particle passes through the magnet structure, the result of the transformation will be a four- dimensional matrix.

For a zero-field drift region,

$$M_{\text{drift}} = \begin{pmatrix} 1 & l & 0 & 0 \\ 0 & 1 & 0 & 0 \\ 0 & 0 & 1 & l \\ 0 & 0 & 0 & 1 \end{pmatrix} \tag{2.19}$$

For a horizontally focusing quadrupole, $k_0 > 0$,

$$M_{\text{QF}} = \begin{pmatrix} \cos\varphi & \frac{1}{\sqrt{k_0}}\sin\varphi & 0 & 0 \\ -\sqrt{k_0}\sin\varphi & \cos\varphi & 0 & 0 \\ 0 & 0 & \cosh\varphi & \frac{1}{\sqrt{|k_0|}}\sinh\varphi \\ 0 & 0 & \sqrt{|k_0|}\sinh\varphi & \cosh\varphi \end{pmatrix} \tag{2.20}$$

For a vertically focusing quadrupole, $k_0 < 0$,

$$M_{\text{QD}} = \begin{pmatrix} \cosh\varphi & \frac{1}{\sqrt{|k_0|}}\sinh\varphi & 0 & 0 \\ \sqrt{|k_0|}\sinh\varphi & \cosh\varphi & 0 & 0 \\ 0 & 0 & \cos\varphi & \frac{1}{\sqrt{k_0}}\sin\varphi \\ 0 & 0 & -\sqrt{k_0}\sin\varphi & \cos\varphi \end{pmatrix} \tag{2.21}$$

By using the solutions of the general equation of motion for each beam line element, we could form transformation matrices for that specific element. Then, we will be able to follow the particle trajectory step by step through the whole transport system along a complicated beam line. In matrix formalism, all we need to do is simply repeating matrix multiplications from one element to another as we follow the particle trajectory. The total transformation matrix M for n magnetic elements and drift spaces is determined by the product

$$M = M_n \cdot M_{n-1} \cdots M_3 \cdot M_2 \cdot M_1 \tag{2.22}$$

This simple model, which is called the "hard-edge model", is widely used to treat most basic beam transport problems. There are many computer code programs, such as Beam Optic[1], which will be used in this research, that use the principle of the hard-edge model. These particle optics simulation codes allow to interactively and visually construct any optical beam line system. They are designed to compute transport matrices, beam envelopes, and trajectories.

In Fig. 2.1, an example of a Beam Optic simulation program for an arbitrary beam line configuration consisting of different quadrupoles, drift spaces, and an alpha magnet is shown.

One important aspect of using such computer simulation codes is the fact that they allow to examine the properties of the selected beam line configuration very quickly. In fact, one could even construct the accelerator system graphically on the computer screen and calculate the properties of the beam line while performing the actual experiment.

It should be noted however, that for such simulation codes to efficiently describe the properties of the beam line, the matrix parameters associated with each element must be correct. The result of these computer code programs would not be realistic if, for example, the quadrupoles suffer from the deviations from the hard-edge model. The hard-edge model is only an approximation, and although for practical purposes a rather good one, in many cases a correction needs to be taken into account [15].

In what follows, we will attempt to derive the appropriate corrections to the hard-edge model.

2.4. Quadrupole End-Field Effect

So far we have only considered the effects of the quadrupole end fringe field in an ideal quadrupole with a constant magnetic field strength in a hard-edge model. However, in a real quadrupole the magnetic field strength does not change suddenly from zero to the full value in a step form function. In reality, the magnetic strength extends well beyond the edge of the iron core and has a smooth transition from zero to a maximum value in the middle of the quadrupole.

---

[1] Originally developed by K. H. Steffens, improved version by Ivan Shvedunov, 2000

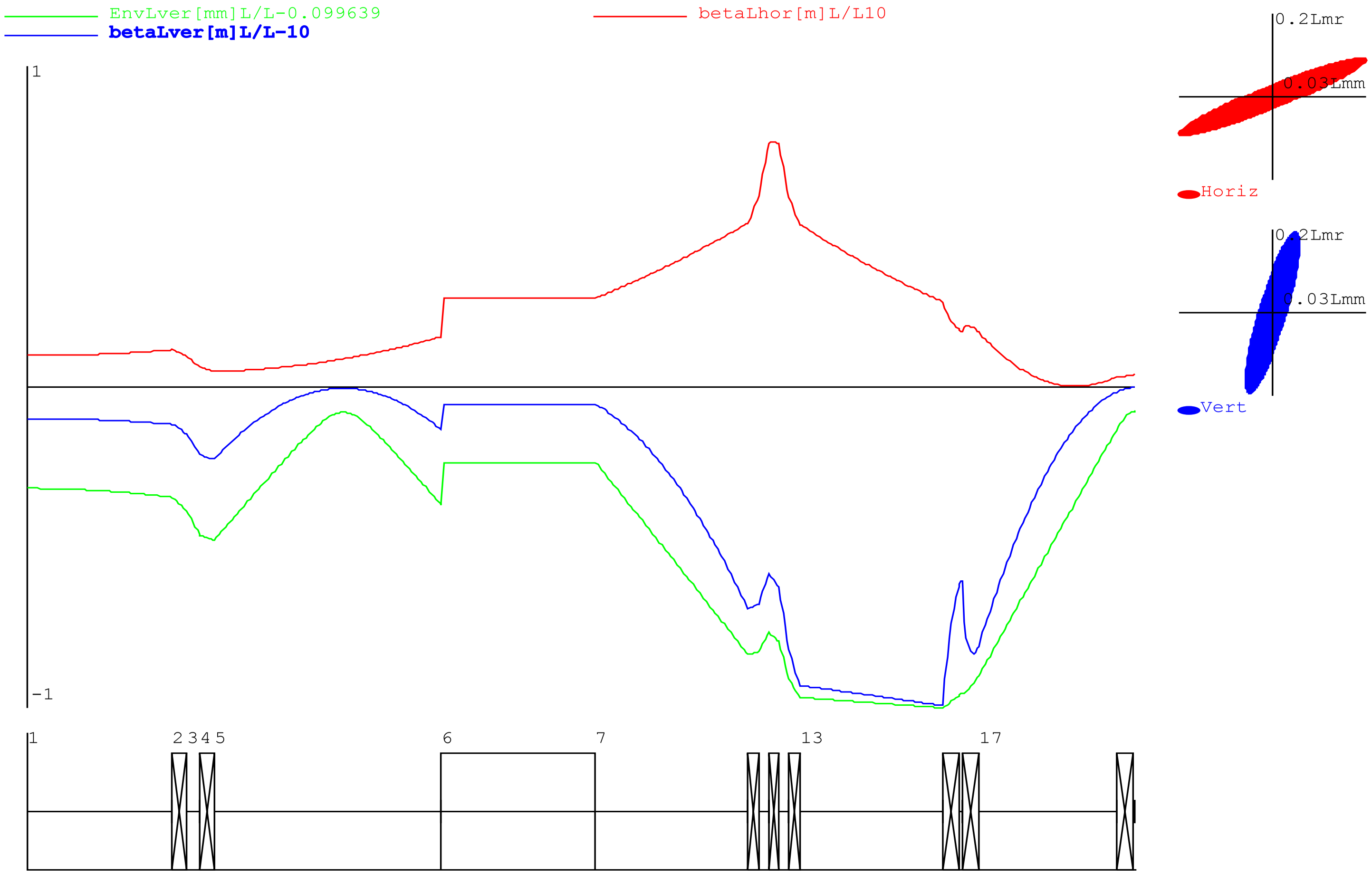

Figure 2.1.: A Beam Optic simulation program showing the result for a beam line constructed by using quadrupole singlet, doublet, triplet, and one α-magnet. The green, red and blue curvatures represent the envelope in vertical direction, and the β-functions (which will be discussed later) in horizontal and vertical directions respectively. The ellipses illustrate the output of the system of the elements.

The magnetic strength of a real quadrupole along the axis is illustrated in the Fig. 2.2.

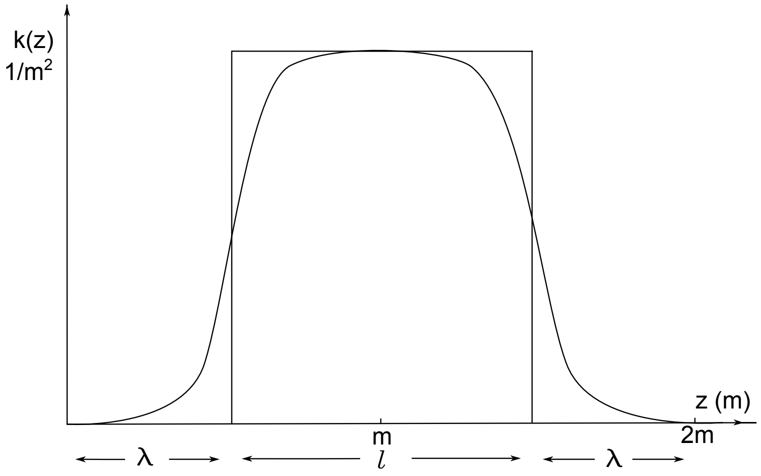

Figure 2.2.: Magnetic field profile in a real quadrupole

Therefore, it is of great importance to make the necessary adjustment to the hard-edge model and bring into account the end field effect of a quadrupole in order to obtain a more accurate transformation matrix.

The real transformation matrix could be obtained, as it is suggested in "Particle accelerator physics" by H. Wiedemann [15], by dividing the whole magnetic field distribution of the quadrupole into small sections of varying strength as shown in Fig. 2.3. Then, treating each of these small sections as a hard-edge quadrupole, one could find the overall transformation matrix by multiplying all the transformation matrices of each individual small quadrupole.

Let us assume that the overall transformation matrix for the real quadrupole resulting from multiplying individual matrices would be in the form of

$$M = \begin{pmatrix} C & S \\ C' & S' \end{pmatrix} \tag{2.23}$$

In order to find the adjustment for the end field effect, we assume that the real, symmetric quadrupole could be replaced with a hard-edge quadrupole of constant effective strength k and effective length l, multiplied by a drift space of length λ on each side [16], as indicated in Fig. 2.2.

The transformation matrix through this system should be equal to the overall transformation matrix M, equation (2.22). By creating this equality, we will be able

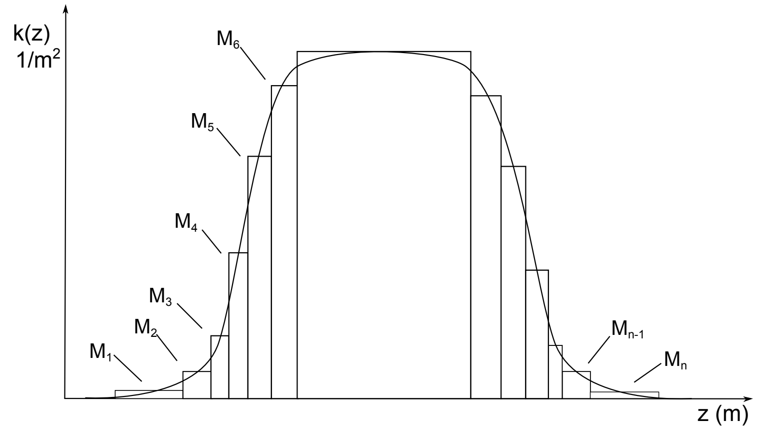

Figure 2.3.: Dividing of the actual quadrupole field profile into small segments of hard-edge quadrupoles

to determine the effective magnetic field strength k, and the effective length l.

$$\begin{pmatrix} C & S \\ C' & S' \end{pmatrix} = \begin{pmatrix} 1 & \lambda \\ 0 & 1 \end{pmatrix} \begin{pmatrix} \cos\varphi & \frac{1}{\sqrt{k}}\sin\varphi \\ -\sqrt{k}\sin\varphi & \cos\varphi \end{pmatrix} \begin{pmatrix} 1 & \lambda \\ 0 & 1 \end{pmatrix} \tag{2.24}$$

$$= \begin{pmatrix} \cos\varphi - \lambda\sqrt{k}\sin\varphi & \lambda\left\{2\cos\varphi + (\frac{1}{\lambda\sqrt{k}} - \lambda\sqrt{k})\sin\varphi\right\} \\ -\sqrt{k}\sin\varphi & \cos\varphi - \lambda\sqrt{k}\sin\varphi \end{pmatrix} \tag{2.25}$$

with $\varphi = l\sqrt{k}$ and introducing m so that $2m = l + 2\lambda$. By using these equalities, we will derive the two equations

$$\cos\varphi^{+} + \frac{1}{2}\varphi^{+}\sin\varphi^{+} = C^{+} - mC'^{+} \tag{2.26}$$

$$l^{+} = -\frac{1}{C'^{+}}\varphi^{+}\sin\varphi^{+} \tag{2.27}$$

where we have used the upper plus sign to emphasize that these parameters are for a focusing quadrupole.

Knowing the values for C^{+} and C'^{+}, the first of these two equations could be solved numerically for φ^{+}, which then could be used in the second equation to determine the value of the effective length, l^{+}, and the effective strength k^{+} for a focusing quadrupole.

Similarly, for a defocusing quadrupole we will obtain

$$\cosh\varphi^- - \frac{1}{2}\varphi^- \sinh\varphi^+ = C^- - mC'^- \tag{2.28}$$

$$l^- = -\frac{1}{C'^-}\varphi^- \sinh\varphi^- \tag{2.29}$$

which will help to uniquely determine the effective parameters l^- and k^-. Equations (2.26) through (2.29) define a hard-edge representation of a real quadrupole.

Customarily, the magnetic field strength, k_0, is the actual value of the magnetic strength in the middle of the quadrupole and the magnetic length is defined by $l = \frac{1}{\sqrt{k_0}} \int k(z)\mathrm{d}(z)$ [14]. However, it is significant to note that the effective quadrupole parameters $l^\pm$ and $k^\pm$ found with this hard edge representation of a real quadrupole are different from the customary definitions of magnetic field strength and length [15]. Furthermore, we observe that the effective quadrupole parameters $l^\pm$ and $k^\pm$ are different for the focusing and defocusing quadrupoles.

In addition, since the end-field effect of a quadrupole depends on the geometrical design parameters of the magnet being used, the effect of the end fields is not the same for all the quadrupoles, and as a result these corrections cannot be determined in general [15].

After one finds all these effective parameters, it is also of interest to determine the relative deviations from the quadrupole effective length and strength,

$$\frac{(\Delta l)^\pm}{l} = \frac{l^\pm - l}{l} \quad \text{and} \quad \frac{(\Delta k)^\pm}{k_0} = \frac{k^\pm - k_0}{k_0} \tag{2.30}$$

and also

$$\frac{\Delta(kl)^\pm}{k_0 l} = \frac{k^\pm l^\pm - k_0 l}{k_0 l} \tag{2.31}$$

which could be used, to calculate the relative fringe field corrections to the quadrupole strength and the quadrupole length [16].

As it is seen from equation (2.30), the quadrupole effective strengths k^+ and k^- are not simply proportional to k_0, but are a function of k_0. This is also true for the quadrupole effective lengths l^+ and l^-, both are dependant on the quadrupole strength k_0. Which means that the magnetic field length is no longer a constant, as it is considered to be customarily.

Therefore, as we take steps to make the necessary adjustments to the hard-edge model, we realize that the conventional values of the magnetic field length and strength are no longer efficient.

In order to factor in the deviations of the effective quadrupole parameters, $l^\pm$ and $k^\pm$, from the conventional values of the magnetic field length and strength and still be able to use the Beam Optic simulation computer program, one must modify the program. This could be done by plugging in the new values into the matrices of the Beam Optic program after determining the field fringe corrections to the quadrupole length and strength. This might require considerable programming effort, but would enable very quick calculations which allow to investigate many configurations of a possible beam line in a short time.

However, it is important to note that in most practical cases [15], these deviations are small for quadrupoles with small aperture, i.e. for the quadrupoles which have a small ratio of aperture to length. On the other hand, these deviations are large for quadrupoles which are small compared to the aperture. The deviations Δl and Δk have opposite polarity [15] and it turns out that in general, the thin lens focal length error $\Delta l \Delta k$ is very small.

2.5. The Quadrupole Doublet

A quadrupole doublet consists of two quadrupoles of the same length that are separated with a drift space d. The quadrupole magnetic gradients in a doublet are equal in magnitude; however, the polarities of the quadrupoles are opposite to each other. Let g_1 and g_2 be the gradient of the quadrupoles in the doublet, then

$$g_1 = -g_2 \tag{2.32}$$

While a single quadrupole focuses in one direction, for example x, and defocuses in the other direction, y, for a quadrupole doublet, depending on the orientation and whether we are examining the x or y direction, we could arrange the quadrupole doublet to be focusing-defocusing, or defocusing-focusing. We shall assume that the first quadrupole is defocusing in the (x, z) plane, and therefore focusing in the (y, z) plane, and that the second quadrupole is focusing in the (x, z) plane , and therefore defocusing in the (y, z) plane.

In matrix formulation, a focusing-defocusing quadrupole doublet of length l separated by a drift space of length d could be presented as

$$M_{\mathrm{FD}} = \begin{pmatrix} \cos\varphi & \frac{1}{\sqrt{k_0}}\sin\varphi \\ -\sqrt{k_0}\sin\varphi & \cos\varphi \end{pmatrix} \begin{pmatrix} 1 & d \\ 0 & 1 \end{pmatrix} \begin{pmatrix} \cosh\varphi & \frac{1}{\sqrt{|k_0|}}\sinh\varphi \\ \sqrt{|k_0|}\sinh\varphi & \cosh\varphi \end{pmatrix} \tag{2.33}$$

where $\varphi = l\sqrt{|k_0|}$.

Similarly, for a defocusing-focusing quadrupole doublet, under the same geometrical configuration, the matrix formulation could be written as

$$M_{DF} = \begin{pmatrix} \cosh\varphi & \frac{1}{\sqrt{|k_0|}}\sinh\varphi \\ \sqrt{|k_0|}\sinh\varphi & \cosh\varphi \end{pmatrix} \begin{pmatrix} 1 & d \\ 0 & 1 \end{pmatrix} \begin{pmatrix} \cos\varphi & \frac{1}{\sqrt{k_0}}\sin\varphi \\ -\sqrt{k_0}\sin\varphi & \cos\varphi \end{pmatrix} \tag{2.34}$$

Multiplying these matrices together, the result for the focusing-defocusing doublet could be written as

$$M_{\mathrm{FD}} = \begin{pmatrix} M_x & L_{\mathrm{eff}} \\ -\frac{1}{f} & M_y \end{pmatrix} \tag{2.35}$$

and similarly for the defocusing-focusing quadrupole doublet as

$$M_{\mathrm{DF}} = \begin{pmatrix} M_y & L_{\mathrm{eff}} \\ -\frac{1}{f} & M_x \end{pmatrix} \tag{2.36}$$

where the focusing or defocusing of the quadrupole doublet depends on the element T_{21} with the equality $T_{21} = -\frac{1}{f}$.

The four matrix elements $\frac{1}{f}$, M_x, M_y, and L_{eff} are given by

$$\frac{1}{f} = \sqrt{k_0}(\sin\varphi\cosh\varphi - \cos\varphi\sinh\varphi + (\sqrt{k_0}d)\sin\varphi\sinh\varphi) \tag{2.37}$$

$$L_{\mathrm{eff}} = \frac{1}{\sqrt{k_0}}(\sin\varphi\cosh\varphi + \cos\varphi\sinh\varphi + (\sqrt{k_0}d)\cos\varphi\cosh\varphi) \tag{2.38}$$

$$M_x = (\cos\varphi\cosh\varphi + \sin\varphi\sinh\varphi + (\sqrt{k_0}d)\cos\varphi\sinh\varphi) \tag{2.39}$$

$$M_y = (\cos\varphi\cosh\varphi - \sin\varphi\sinh\varphi - (\sqrt{k_0}d)\sin\varphi\cosh\varphi) \tag{2.40}$$

As we see from these equations, the transformation matrices in the x and the y directions are not equal however, the focusing i.e. T_{21} element, in both directions are equal.

2.6. The Phase Space Ellipse and the Twiss Parameters

Before we describe the research approach and the experiment, it seems appropriate to briefly explain the phase ellipse and its parameters. To describe the beam as a whole without concentrating on individual particle trajectories in phase space, we can surround all the particles of a beam in phase space by an ellipse [14].

If one has the knowledge of the phase space that is occupied by the charge particles at the beginning of the beam line, then we could determine the distribution and location of the beam at any other place of the beam transport line. The ellipse, shown in Fig. 2.4, that encloses all the particles of the beam in the phase space is called phase ellipse, which could be described in the (x, x') plane as

$$\gamma x^2 + 2\alpha x x' + \beta x'^2 = \epsilon \tag{2.41}$$

where α, β, γ, and ϵ are the ellipse parameters.

α, β, and γ, which are called Twiss parameters, determine the shape and also the orientation of the ellipse. α is related to the phase ellipse orientation, β is related to the beam shape and size, and γ is dependent on α and β. ϵ is the beam emittance and is proportional to the area of the phase ellipse by the equation $A = \pi\epsilon$ [14]. These parameters satisfy the condition

$$\beta\gamma - \alpha^2 = 1 \tag{2.42}$$

Liouville's theorem [13] states that the area of the phase ellipse and therefore the emittance remains constant throughout the beam transport line assuming that

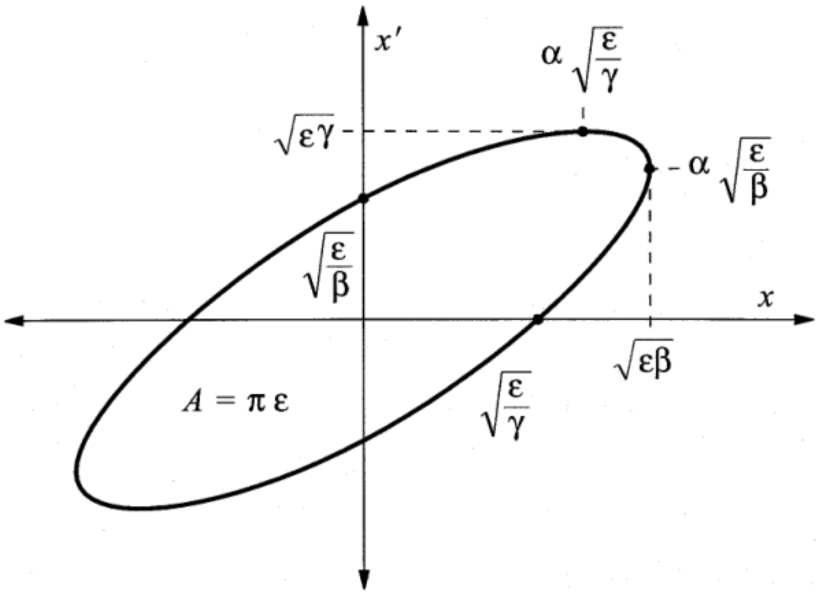

Figure 2.4.: The phase space ellipse of a particle motion in the (x, x') plane [13]

the particles obey the canonical equations of motion, which is satisfied in our case. Preservation of the areas in the phase space therefore requires that the determinant of all two-dimensional matrices be equal to one.

2.7. The Electron Optical Properties of the Wien Filter

In the time resolved polarization experiments, by applying a short optical laser pulse of the order of magnitude of the picosecond or femtosecond, the valance electrons in the semiconductor will be excited to the conduction band. This excitation process will initialize the spin orientation. Subsequently, the evolution of the degree of spin polarization of the electrons could be measured.

In order to perform the time resolved spin polarization measurements, which is planned to be conducted in the PKAT beam transport system following the current project, the originally longitudinally polarized electrons must be transformed to the transversally polarized. These measurements, which are done through a Mott polarimeter, necessitate the use of a spin rotation system like the Wien filter.

A Wien filter is a compact spin rotator system that consists of homogeneous electric and magnetic fields which are perpendicular to each other and transverse to the direction of the particle motion. A cross section of the Wien filter is illustrated in Fig. 2.5.

In the Wien filter, two parallel electrostatic condenser plates produce the electric

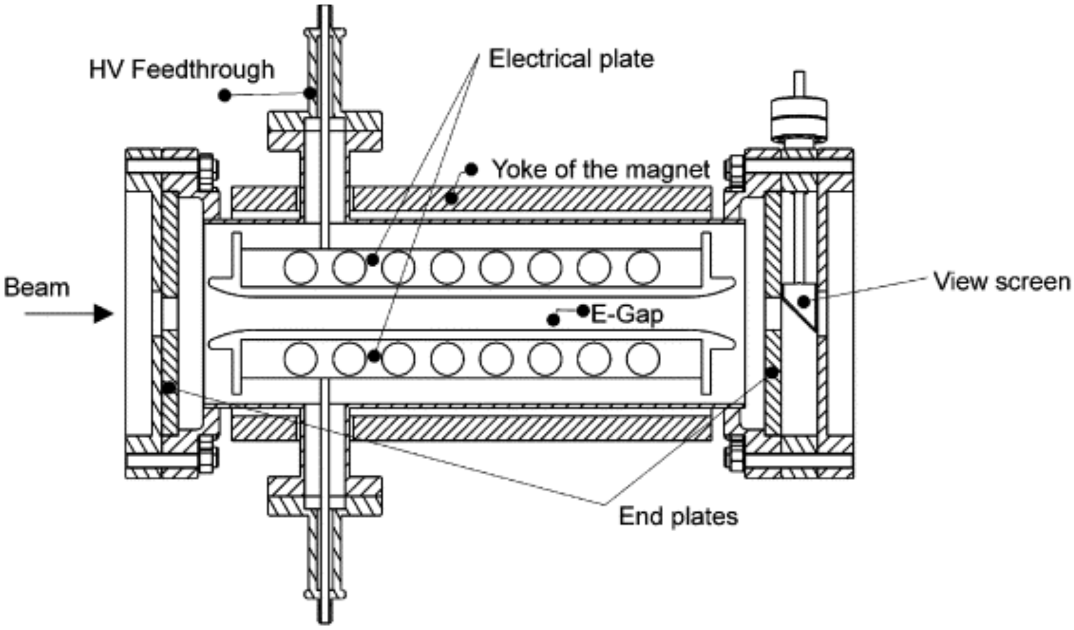

Figure 2.5.: Cross section of the Wien filter [13]

field. Providing a symmetrical voltage supply to the two plates ensures that the zero-voltage equipotential lines coincide with the symmetry axis of the condenser. These plates are arranged between magnetic poles to create homogeneous electric and magnetic fields crossing each other. The magnetic field is produced by a magnet of the "window frame" type [13].

As the charged particle with the velocity $\boldsymbol{v}$ travels through the Wien filter, it will go through the electric and magnetic field associated with the Wien filter. Therefore, to achieve the condition of no deflection from the reference beam trajectory, the electric and magnetic field of the Wien filter, must satisfy the relationship

$$\boldsymbol{B} \times \boldsymbol{v} = \boldsymbol{E} \tag{2.43}$$

In the time resolved polarization experiments the electrons undergo a spin precession due to the magnetic field according to the Thomas-BMT equation [17]. Therefore, the condition of $\boldsymbol{B} \times \boldsymbol{v} = \boldsymbol{E}$ must also be fulfilled even while the values of the fields are varying in order to achieve the desired angle of the spin rotation for the electrons.

Assume that the electrons are moving along the z-axis, the electric field is directed along the x-axis, and that the magnetic field is in the y direction. When the condition of no deflection for the electrons in equation 2.43 is fulfilled, the first order approximation of the transformation matrix for the horizontal motion could be expressed by the following matrix [18].

$$T = \begin{pmatrix} \cos(L/R) & R\sin(L/R) & -R(1-\cos(L/R)) \\ -R^{-1}\sin(L/R) & \cos(L/R) & -\sin(L/R) \\ 0 & 0 & 1 \end{pmatrix} \tag{2.44}$$

where $R = \gamma mv/eB$, and L is the field effective length. We have assumed that the entrance and the end fringe field regions are short compared to the length of the device. In the vertical direction, y, there is no focussing action by the Wien filter, therefore, the corresponding y matrix is only a drift space [18].

By using a Wien filter, it is possible, in practice, to achieve reliable spin rotation for an angular range of $\pm\frac{\pi}{2}$. For a $\frac{\pi}{2}$ spin rotation, that will correspond to

$$\frac{\pi}{2} = \frac{mc\beta\gamma}{eBL} \tag{2.45}$$

or simply, $\frac{\pi}{2} = \frac{L}{R}$. Since the effective field length of the Wien filter is $L = 0.32\,\mathrm{m}$, that will lead to $R = 0.20\,\mathrm{m}$, which results to the transformation matrix element M_{21} to be $M_{21} = 4.91\,\mathrm{m}^{-1}$.

By reversing the field directions, the negative values of the spin rotation are easily obtained. Furthermore, the spin orientation may be flipped by reversing the source laser helicity [19]. Therefore, any desired spin orientation in the plane of the accelerator can be achieved [13].

3. Research Approach and Experiment I

As already mentioned, one of the basic building blocks of a charged particle beam transport system are the quadrupoles, which serve as a focusing device to keep the particle beam close to the desired beam path. Most quadrupole magnets which are built for beam transport lines are electromagnets [14]. This means these magnets are excited by electrical current going through the coils wrapped around the magnet poles.

The main objective of this section is to find the current at which the quadrupole could produce the best focused beam.

3.1. Large Aperture Quadrupoles

Since the quadrupoles that are planned to be used right after the source injector system in the construction of MESA, in the low energy area (up to 5 MeV), are large aperture quadrupoles, it is of great importance to study these quadrupoles in depth. These large aperture quadrupoles have a ratio of aperture to length as high as almost one. For the construction, and therefore the operation of MESA to be successful, it is extremely important to make sure that the quadrupoles right after the source injector are properly designed and carefully constructed in the beam line of MESA.

In addition, since the existing quadrupoles in the MAMI injector system have also large aperture, we could instead study these large aperture quadrupoles and characterize their end-field effect.

However, PKAT beam transport system uses the same large aperture quadrupoles. Furthermore, the time resolved spin polarization measurements, which will be performed in the PKAT following the completion of this project, require the use of spin rotator Wien filter. In lieu of the fact that the Wien filter has a very strong quadrupole component in one direction, we must compensate for the strong quadrupole component of the Wien filter. Therefore, we will shift our focus on investigating only the quadrupoles in the beam line of PKAT. In Fig. 3.1 the design of the PKAT beam line system is shown.

PKAT is a low energy beam transport system which houses 7 large aperture quadrupoles, along with other magnetic elements, such as steering magnets and 2 α-magnets. The source injector system of MESA plus a few elements right after that, such as the quadrupoles and the α-magnet, will be exactly similar to that of PKAT. Therefore, in order to effectively construct the needed large aperture quadrupoles into the MESA accelerator system and in preparation for the time

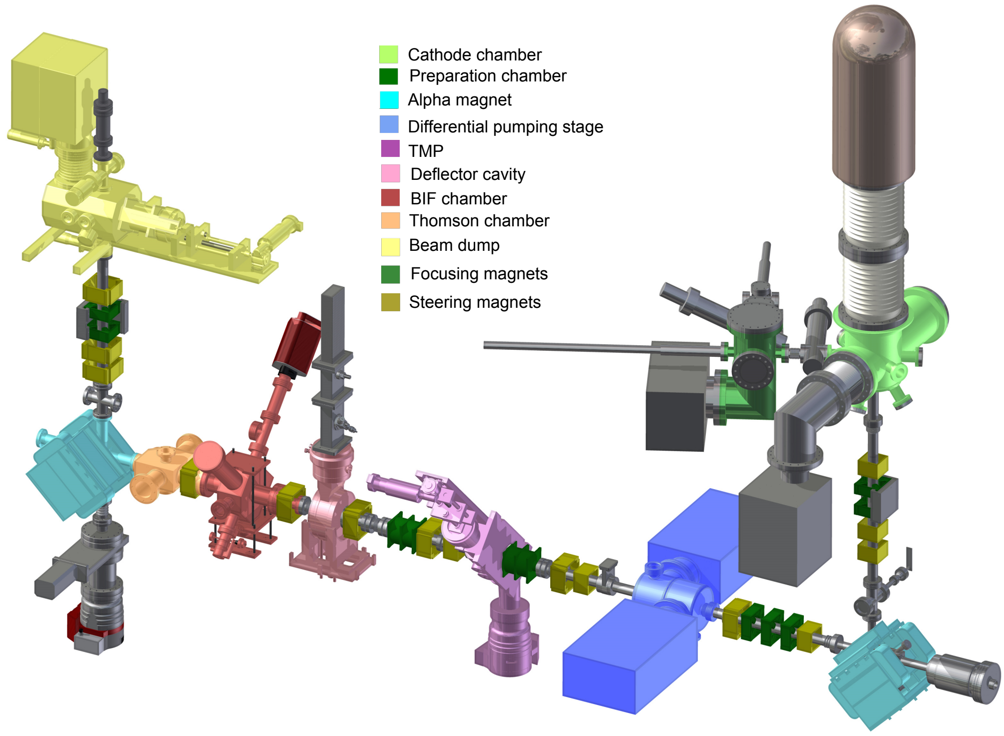

Figure 3.1.: The design of the PKAT beam line transport system

resolved polarization measurements with the use of the Wien filter, we have decided to investigate the quadrupoles in the PKAT beam transport system.

A close up section of the PKAT after the planned installation of the Wien filter for the time resolved polarization measurements is illustrated in the Fig. 3.2.

In particular, for the moment, our focus is on studying only the quadrupole number 3, the first quadrupole in the PKAT beam line. The reason for investigating only this quadrupole is simply that, if we are able to understand how one quadrupole functions and predict its behaviour in the beam line, then we can take this information and apply it to a more complicated beam line made of many quadrupoles and other elements.

Although our goal is to investigate one quadrupole and be able to ideally apply the results to the other quadrupoles, we have to keep in mind that the quadrupoles built into the beam transport system of the PKAT are of different origin. These quadrupoles have different design since some were built with different number of windings and thus have unknown quadrupole strengths.

We achieve the goal of finding the current for the best focused beam by using two different approaches: First, by considering the quadrupole as a hard-edge quadrupole with an effective length l_{eff} and second, by implementing the improved treatment of the quadrupole end effect and using the matrix transformation for the quadrupole.

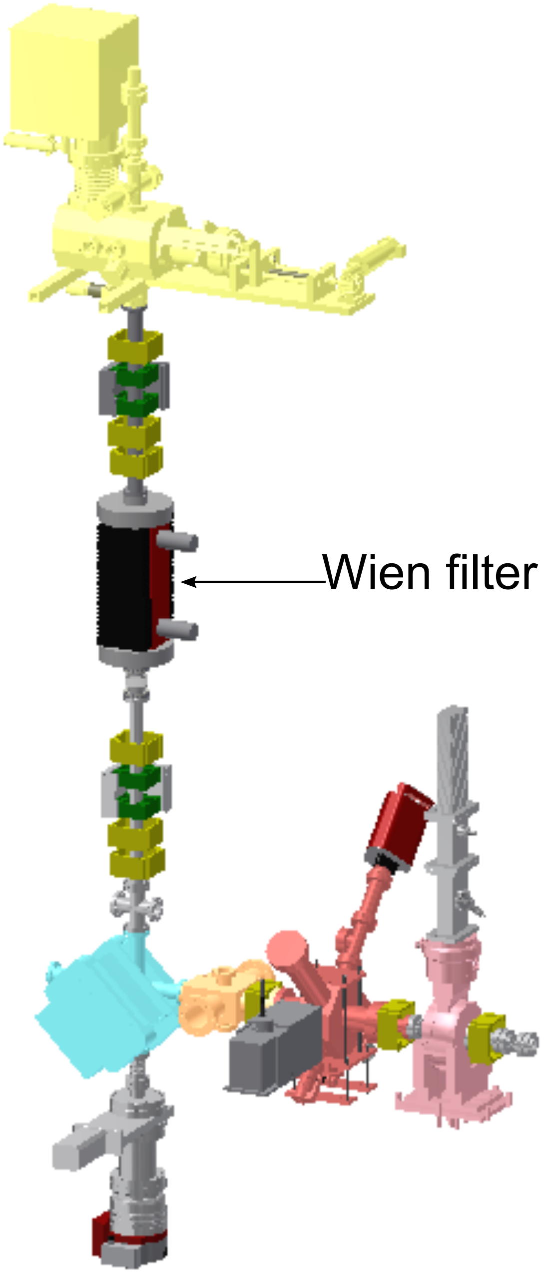

Figure 3.2.: The design of the section of the PKAT beam line transport system after installing the Wien filter for the time resolved polarization measurements

In both of these approaches, there are some parameters needed to enter in the Beam Optic computer simulation program. The first of which, are the Twiss parameters, α, β, and γ, for the source which are taken from [20].

$$\alpha = -1.05 \qquad , \qquad \beta = 0.23\,\frac{\mathrm{mm}}{\mathrm{mrad}} \qquad , \qquad \gamma = 9.31\,\frac{\mathrm{mrad}}{\mathrm{mm}} \tag{3.1}$$

Also, the values for the emittance, which are considered to be one.

In addition, we need to know the distances between the source and the quadrupole, and from the quadrupole to the screen, where we observe the size of the beam.

In both of these methods, our strategy is by knowing the distances from the quadrupole to the source and to the screen, also by having the Tiwss parameters for the source and the quadrupole parameters, we use the computer simulation program, Beam Optic, to obtain the size of the beam, which then will be used to determine the current necessary to achieve the best focused beam.

Now, in what follows we will discuss these two approaches in detail. The first one is discussed in this chapter and the second approach will be the subject of the next chapter.

3.2. Hard-Edge Quadrupole

In this approach, the quadrupole is a hard-edge quadrupole with the gradient having a step-form function. In order to use the first approach and find the current for the focused beam size, we need to know the value of the quadrupole magnetic strength. If one knows the magnetic field distribution in the center of the quadrupole then the magnetic field gradient g, and therefore the quadrupole magnetic strength k can be determined.

It must be noted that in the Beam Optic simulation program, the coding for the k-quadrupole stands for the kl_{eff}. Therefore, after finding the magnetic strength, k, one must multiply it by the l_{eff} before entering it in the Beam Optic computer simulation program. Following this approach then is contingent upon having the magnetic field distribution in the center of the quadrupole.

However, since the quadrupoles are fixed in the PKAT beam line, one cannot access the volume at the center of them to measure the shape of the magnetic field directly. We can only measure the magnetic field in the limited area of the fringes of the quadrupoles due to the fact that the quadrupoles cannot be disassembled for the following reasons:

In order to measure the magnetic field in the center of the quadrupoles, it is not desirable to break the ultra-high vacuum. The ultra-high vacuum condition of 1×10^{-11} mbar in that section of the PKAT beam line system requires the process of baking out, which is tedious. Achieving such ultra-high vacuum is obtained by increasing the temperature of the vacuum tube to 150 °C, while the quadrupole coils must not be heated above 80 °C. If the vacuum condition were to break, the process of baking out would demand special precautions which are necessary to avoid destroying the quadrupole coils by the heating coils.

In addition, the process of the bake out by itself is very time consuming. Even if in the process of breaking the vacuum, removing and replacing the quadrupoles, and the baking out nothing breaks, this will require at least one month of shut down time for the PKAT. Considering that the PKAT beam line system has been built more than 20 years ago, and the fact that in the course of the bake out there is a great possibility that the quadrupole heating protectors might, as a result, easily break, this process, in reality, could cause a much longer time of shut down for the PKAT.

Therefore, due to the fact that breaking the vacuum is not desirable and that the only area accessible to measure the magnetic field is in the fringe of the quadrupoles, in order to overcome this problem, the following strategy is taken.

3.2.1. Reference Quadrupole

In order to determine the value of the magnetic field in the center of the quadrupoles, the first step is finding another quadrupole, called "reference quadrupole", which has very identical quadrupole parameters as compared to the quadrupoles in the PKAT beam line system.

Our method to verify whether the reference quadrupole has the same parameters as the PKAT quadrupoles is by measuring the magnetic field in a very specific orientation and position in the fringe areas of all these quadrupoles. If these measured magnetic fields are the same for that specific orientation and position, one can conclude that the value of the magnetic field in the center of these quadrupoles will be the same as well. Then, we could simply use the parameters of the reference quadrupole in place of the parameters of the quadrupoles in the PKAT to enter into the Beam Optic program in order to find the size of the beam.

The steps to choose the reference quadrupole are as follows: First, the resistances of all the quadrupoles in the PKAT beam line were measured. Then, we found three other quadrupoles, which were previously numbered as 44, 45, and 46, to check which one could be qualified to be chosen as the reference quadrupole. The measured values for the resistance of all these quadrupoles are listed in Table 3.1.

Table 3.1.: Resistance of the 7 quadrupoles in the PKAT system and the 3 quadrupoles under test

Quad	3	4	8	9	10	26	27	44	45	46
$R(\Omega)$	8.56	1.88	3.58	8.46	3.56	8.51	8.55	8.62	8.63	8.68

In this table, the specific numbers chosen for the quadrupoles are based on how these elements are identified in the PKAT beam line system. As it is seen in the above table, the resistance of all the three quadrupoles under test are very close to each other and to the resistance of the majority of the quadrupoles in the PKAT.

Next, for each of these three quadrupoles, the place of $B = 0.0\,\mathrm{T}$ was found by using a set-up which consists of two micrometers moving perpendicular to each other in the x and y directions. The Gaussmeter probe was attached to the micrometer set-up in a fixed position. In Fig. 3.3, the picture of the magnetic probe attached to the two perpendicular micrometers entering the quadrupole under test can be seen.

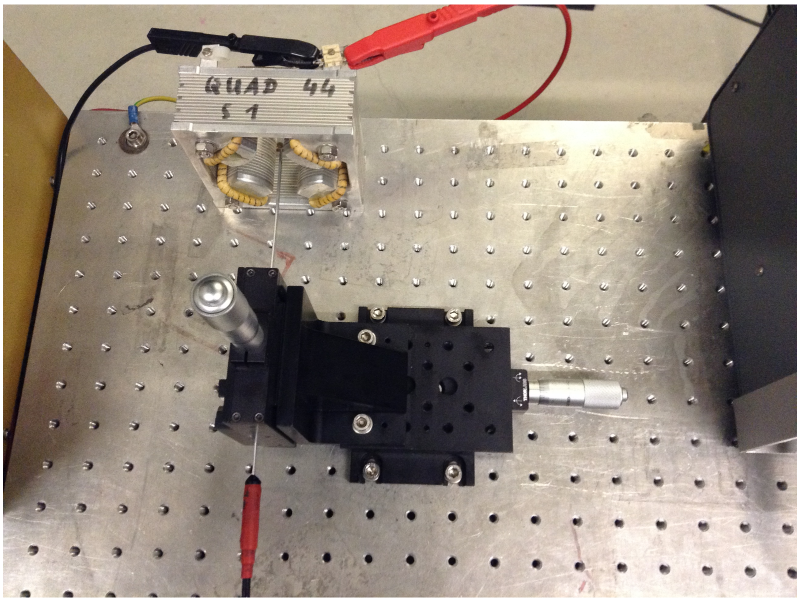

Figure 3.3.: The two perpendicular micrometers used to find the location of $B = 0.0\,\mathrm{T}$

After taking the necessary precaution steps of making sure the zero of the Gaussmeter was adjusted, and that the probe was set in such a way to exactly enter the quadrupole horizontally, the current was set at an arbitrary value of $I = 0.4\,\mathrm{A}$. Then, the exact center point of the quadrupole at which the magnetic field was zero in both horizontal and vertical directions was found. Next, the magnetic probe was moved to a fixed, but arbitrary position from the position of $B = 0.0\,\mathrm{T}$, corresponding to the magnetic center of the quadrupole, and the magnetic field for various currents, ranging from $I = 0.0\,\mathrm{A}$ to $0.9\,\mathrm{A}$ for each of the three quadrupoles under test was measured. Fig. 3.4 represents the result of these measurements.

As it can clearly be seen in this graph, these three quadrupoles under test show very similar behaviour, and their magnetic field properties are in close agreement with each other. The deviation between the magnetic field of the quadrupole 44 and the other two quadrupoles, which reaches almost 5 % at the highest, is perhaps the result of the error in the measurement and not having enough accuracy in finding the place of the $B = 0.0\,\mathrm{T}$.

Since the resistance of the quadrupole number 44 is the closest to the resistance of the majority of the quadrupoles in the PKAT beam line system, it seems that quadrupole number 44 would be a good candidate to be chosen as reference quadrupole. So for now, we decide to choose quadrupole number 44 as our reference quadrupole.

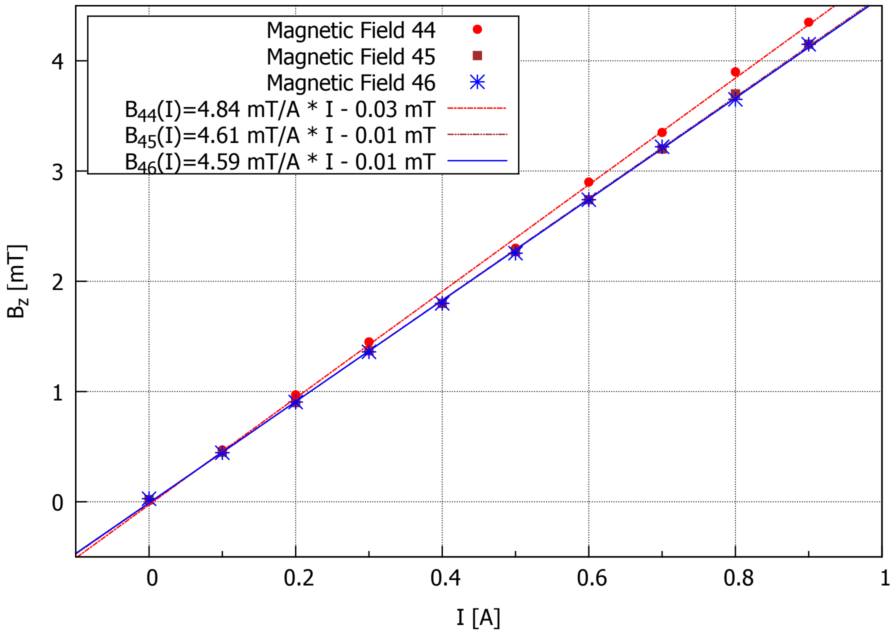

Figure 3.4.: The variation in the magnetic field as a function of current for the three quadrupoles under test

The final determination, however, would be after measuring the magnetic fields in the fringes of all the quadrupoles in the PKAT and the quadrupole 44 and observing how close these measurements are to each other.

3.2.2. Measuring the Magnetic Field of the Reference Quadrupole and the Quadrupoles in the PKAT

As we discussed earlier, the only accessible space, in which the magnetic field of the quadrupoles in the PKAT transport system could be measured, is in the fringes of the quadrupoles. In order to measure the magnetic field in a specific orientation and position, a device was constructed so that the probe for measuring the magnetic field could be inserted in the quadrupole at a 45° angle. In Fig. 3.5 the inaccessible space in the center of the quadrupole as well as the close-up of this device entering in the reference quadrupole at the 45° angle are illustrated.

With the probe being inserted the quadrupole at 45° in a specific position, and for a fixed current of $I = 1.0\,\mathrm{A}$, the magnetic fields of the reference quadrupole and each of the quadrupoles in the PKAT beam line system were measured. In each of these measurements, to be certain that the measurements were consistent, we made sure that our device was sitting flush to the underneath part of the quadrupole as it can be seen in Fig. 3.5.

For the reference quadrupole, since we had the freedom of inserting the probe from each four sides and even rotating the quadrupole to observe whether the earth's mag-

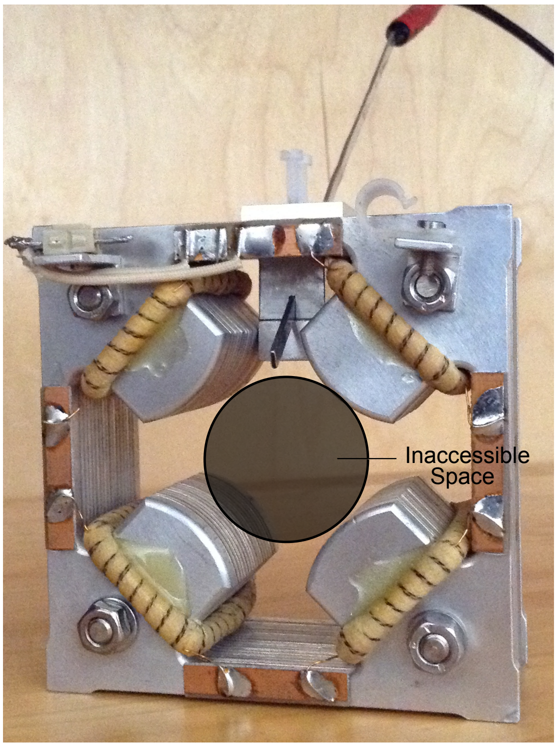

Figure 3.5.: The magnetic probe entering the quadrupole at a 45° angle. The dark circle represents the space which is inaccessible to make measurements.

netic field would cause any effect on the measurements, multiple measurements were performed. However, for the actual quadrupoles in the PKAT beam line system, since they are fixed in the PKAT and because of the limited access area to be able to insert the probe in that specific orientation and position, the probe could be inserted only in one or two positions, depending on the accessibility of the surrounding environment of the quadrupole.

For each position of the probe, the measurements for the magnetic field were repeated three times. These values were averaged and put together in Fig. 3.7. In this graph, as mentioned earlier, the specific numbers chosen for the quadrupoles are based on how these elements are identified in the PKAT transport system. Also, the green linein the graph, at $B = 9.20\,\mathrm{mT}$, indicates the average magnetic field for the tested reference quadrupole 44 at 45° angle.

It is important to note, as it is clearly seen in Fig. 3.7, that the magnetic fields of the quadrupoles numbers 3, 9, 26, and 27 are close to each other. Therefore, one could put these quadrupoles in one group. Similarly, quadrupoles numbers 4, 8, and 10 could be put together in another group.

Comparing the average magnetic field of the tested reference quadrupole with of the quadrupole 3 we see that the magnetic field of the quadrupole 3 has an error

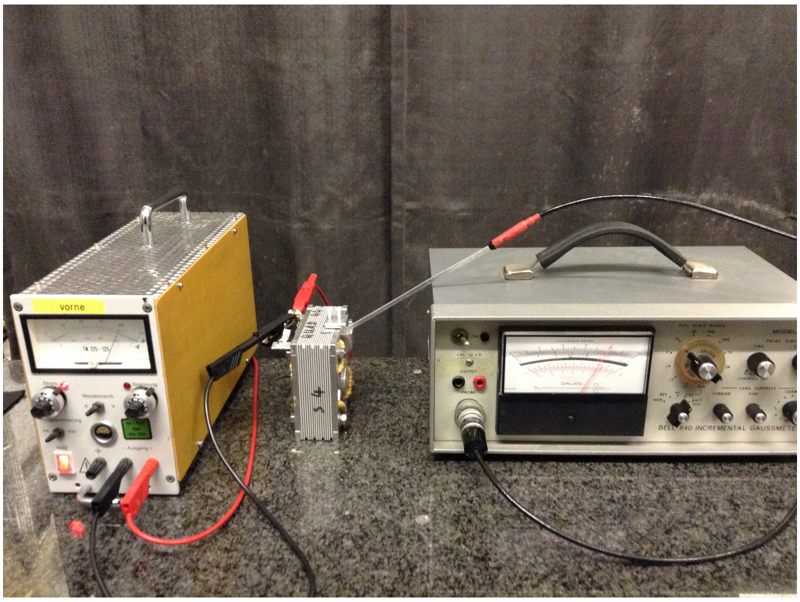

Figure 3.6.: The set-up for measuring the magnetic field of the reference quadrupole and the quadrupoles in PKAT at a 45° angle

of 5.3 % at the highest and 0.9 % at the lowest as compared to the magnetic field of the reference quadrupole. If we just consider the average magnetic field of the quadrupole 3, $B = 9.4\,\mathrm{mT}$, the error would be at 2.2 %.

Since the average magnetic field measurement for the reference quadrupole is $B = 9.20\,\mathrm{mT}$, the close agreement of the measured magnetic field of this quadrupole under test and the quadrupoles numbers 3, 9, 26, and 27 is a confirmation that quadrupole number 44, indeed, could be chosen as the reference quadrupole, and that its quadrupole parameters could be inserted in the Beam Optic program in place of the parameters of those quadrupoles in the PKAT beam line to find the minimum beam size. For the remaining quadrupoles in the PKAT, quadrupoles 4, 8, and 10, we will use the proportionality of their magnetic field to the magnetic field of the reference quadrupole.

3.2.3. Measuring the Magnetic Field Gradient of the Reference Quadrupole

In order to measure the magnetic field gradient of the reference quadrupole, the set-up with the two micrometers moving perpendicular to each other, which was used in section 3.1.1 and can be seen in Fig. 3.3, is used. After making sure that the probe will enter the quadrupole horizontally, the current is set at $I = 0.800\,\mathrm{A}$, and then, the exact center point of the quadrupole at which the magnetic field is zero in both horizontal and vertical directions is found.

In addition, while the current is fixed, the magnetic field at the point where the

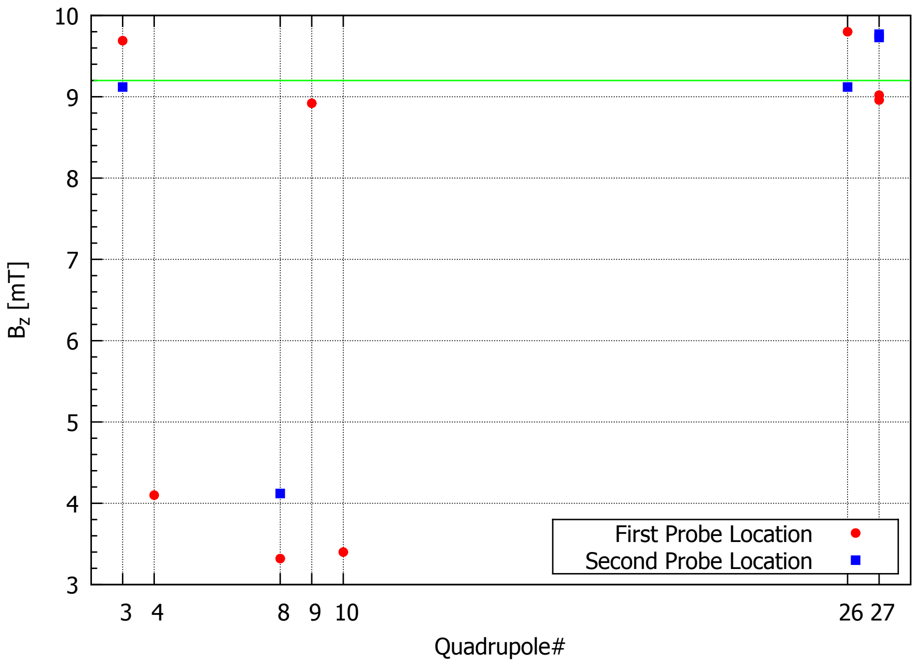

Figure 3.7.: The average magnetic field of the quadrupoles in the PKAT for I=1.0 A. The average value of the magnetic field for the reference quadrupole 44 is illustrated by the green line.

probe is moved 1.0 cm up from the position of $B = 0.0\,\mathrm{T}$ is obtained. The measured value at this point is $B = 3.7\,\mathrm{mT}$ for the current $I = 0.800\,\mathrm{A}$. Then, the probe is moved in increments of 0.5 cm, horizontally, inward and outward the quadrupole in the z direction, and in each position the magnetic field is measured. These measured values are plotted in Fig. 3.8.

It should be mentioned that the reason for not having too many measurements, as we move the magnetic probe in and out of the quadrupole, is because the purpose of the research at this time is not finding a complete distribution for the magnetic field, but it is merely verifying whether the location of the $B = 0.0\,\mathrm{T}$ is accurate.

From these measurements, one can immediately determine the magnetic field gradient for the reference quadrupole, which for $I = 1.0\,\mathrm{A}$ is

$$g = (4.63 \pm 0.05)\,\frac{\mathrm{mT}}{\mathrm{cm}} \tag{3.2}$$

In this measurement, the errors associated with the accuracy of finding the location of the $B = 0.0\,\mathrm{T}$ and the alignment of the magnetic probe in the horizontal direction, and also the calibration of the instruments have contributed to the error of the magnetic field gradient. Comparing this field gradient with the result found by Karl H. Steffens [21], we see that our measurement is in excellent agreement, 0.1 %, with his.

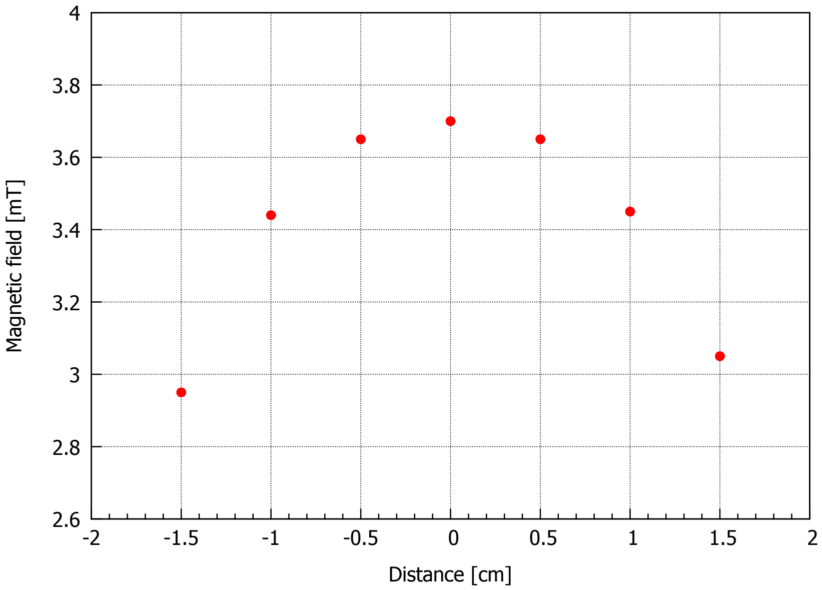

Figure 3.8.: Magnetic field as a function of distance for the reference quadrupole at the current $I = 0.800\,\mathrm{A}$

3.3. Finding the Focused Beam Size Using the Magnetic Field Gradient

The Beam Optic computer program is designed to study the effect of the optical elements on the beam. To be able to observe the beam behaviour throughout the beam line system and determine the size of the beam, one has to enter the parameters for the source and also for each of the elements being used into the Beam Optic program.

To further narrow down the focus of our research, for the moment, our interest is investigating only the quadrupole number 3, the first of the seven quadrupoles in the PKAT beam line transport system. This means that the spaces from the anode and the screen to the quadrupole 3 are considered to be drift spaces. Later on, in Chapter 5, we will expand our research to study the first quadrupole doublet in the PKAT beam line, i.e. quadrupoles 3 and 4.

The close up picture of the location of the source, anode, quadrupole 3, and the screen, which provides means of observing and measuring the size of the beam, can be seen in Fig. 3.9.

In order to use the Beam Optic computer simulation program and find the size of the beam at the screen located right after quadrupole number 3, we need to know the Twiss parameters of the source, the quadrupole strength for the specific current, and the length of the two drift spaces from the anode and the screen to the quadrupole, (Drift 1) and (Drift 2), respectively.

The distance from the anode to the center of the quadrupole is measured as

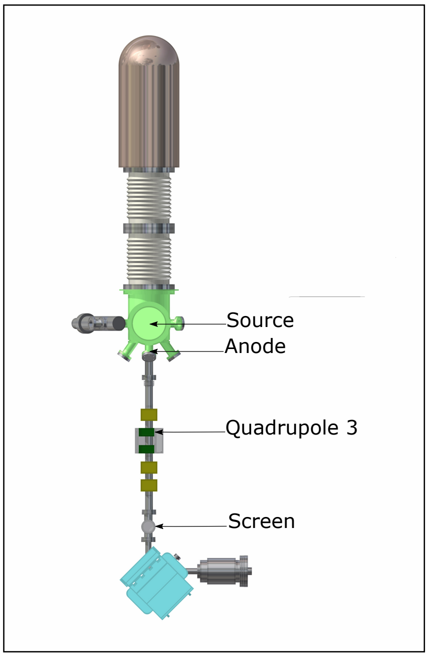

Figure 3.9.: The close-up locations of the source, anode, quadrupole 3, and the screen in the PKAT beam transport system

44.25 cm, and 56.45 cm from the center of quadrupole to the screen. It should be noted that in determining the distance from the anode to the center of the quadrupole, we have assumed the following values:

- The distance from anode to the center of the quadrupole = 44.25 cm
- The width of the quadrupole = 4.1 cm, and
- The adjustment for the new source, since the new source sits 5.0 cm higher than the previous one [22].

Since the quadrupole is considered to be a hard-edge quadrupole with an effective length of $l_{\text{eff}} = 48\,\text{mm}$ [21], the values of the two drift spaces could be determined precisely by using the information mentioned above. This will result in

$$\text{Drift1} = 46.85\,\text{cm} \quad \text{and} \quad \text{Drift2} = 54.05\,\text{cm} \tag{3.3}$$

Finally, by having the magnetic field gradient, the magnetic strength of the quadrupole for each specific current can easily be obtained using the equality $k = \frac{e}{p}g$. Since the kinetic energy of the electrons in the PKAT beam transport system is $E_k = 100\,\text{keV}$, the momentum of the electrons can be computed by applying the relativistic relations.

Then, by using the Beam Optic simulation program, and entering the parameters for the source from equations (3.1), the values for the emittance, the length of the two drift spaces, and the magnetic strength of the quadrupole for each current, the size of the beam can be determined.

In the Beam Optic simulation we have chosen the k-quadrupole for quadrupole 3, recalling that the coding for the k-quadrupole requires a parameter, which is a multiplication of the magnetic strength by the effective length, kl_{eff}. Then, by changing the current, which changes the magnetic gradient, and repeating the steps mentioned above, we can find the variation of the beam size as a function of the current for a hard-edge quadrupole. These variations are put together in the Appendix A.1 and are displayed in Fig. 3.10.

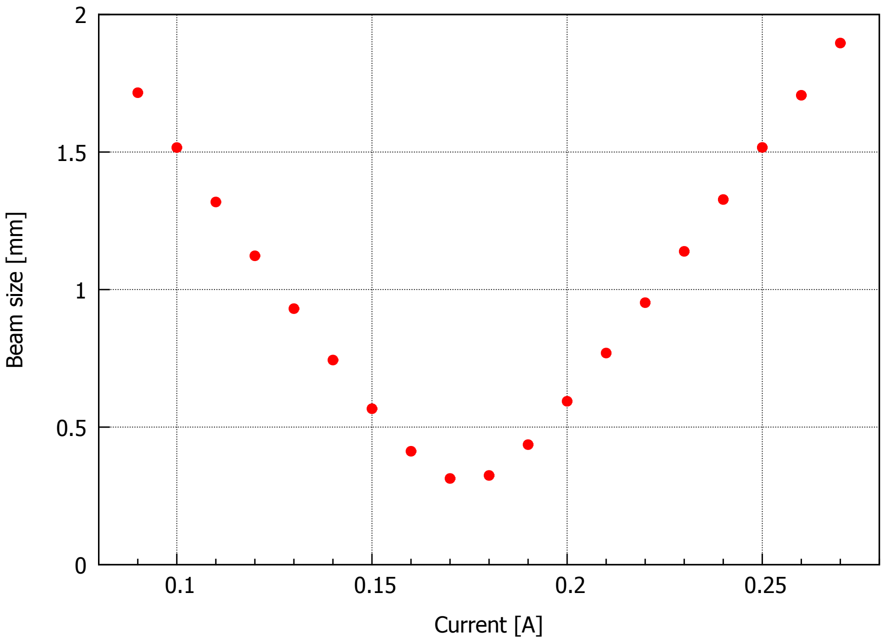

Figure 3.10.: The size of the beam as a function of current for a hard-edge quadrupole

Based on these measurements, as Fig. 3.10 indicates, the best focused beam for the hard-edge model is obtained at about $I = 0.17\,\text{A}$.

In the following chapter, we will discuss the second approach to our research by improving the treatment of the end-field effect and based on that approach will obtain the current which yields the most focused beam. Later on, at the end of the chapter, we will compare the two results of our computer simulation programs with the experimental value of the current at the time of having the best focused beam.

4. Research Approach and Experiment II

In the previous chapter, we had considered the hard-edge model for the quadrupole under study. In doing so, we had assumed the quadrupole to be an ideal quadrupole with a constant magnetic field gradient and with the effective length $l_{\text{eff}} = 48\,\text{mm}$. However, since the magnetic field distribution of a quadrupole has in fact a smooth transition that extends far beyond the edge of the quadrupole, as it is seen in Fig. 2.2, in reality, the customary definitions of quadrupole strength and effective length are not efficient.

In view of the fact that the quadrupole under study, as well as those in the injection system of MAMI, the PKAT beam line, and also the quadruples planned to be used in the construction of MESA, all have a high ratio of aperture to length, a modification to the conventional beam transport analysis must be made [15]. Therefore, depending on the excitation of such quadrupoles, a correction to the quadrupole strength and effective length is required.

The subject of this chapter is to include the quadrupole end field effect in our calculations more thoroughly, and determine the proper transformation matrix for the quadrupole. In doing so, we use the method of dividing the quadrupole field gradient distribution into small sections. Then, we insert the obtained matrix parameters in the Beam Optic program to investigate the necessary current to achieve the most focused beam.

4.1. Transformation Matrix by Dividing the Quadrupole into Small Sections

4.1.1. Finding the Quadrupole Overall Transformation Matrix

Following the approach we discussed in chapter 1, to have an improved treatment for the quadrupole end effect and find the true quadrupole strength and effective length for a focusing quadrupole, the first step is dividing the magnetic field gradient distribution into many small sections. Next, by treating each section as a small hard-edge quadrupole the overall transformation matrix can be calculated.

In order to divide the magnetic field distribution into small sections, we will use the gradient data measured by S. Heidrich [23]. This data was obtained using a large aperture quadrupole similar to the reference quadrupole in our project. Heidrich had measured the magnetic field for a 10 cm interval, which is well beyond the edge of the quadrupole.

Since this gradient data has only a total of 57 data points, by using the "Spline" in the "Octave" computer program we will estimate all the intermediate values in between the data points and obtaine a continuous magnetic field gradient distribution. Fig. 4.1 illustrates the continuous gradient distribution of the original 57 data points. In this graph, the black lines show the outline of the hard-edge quadrupole with the effective length $l_{\text{eff}} = 0.048\,\text{m}$. The small asymmetry at the left tail of the graph as compared to the right side is resulted from the original gradient data points which was used in the Spline program.

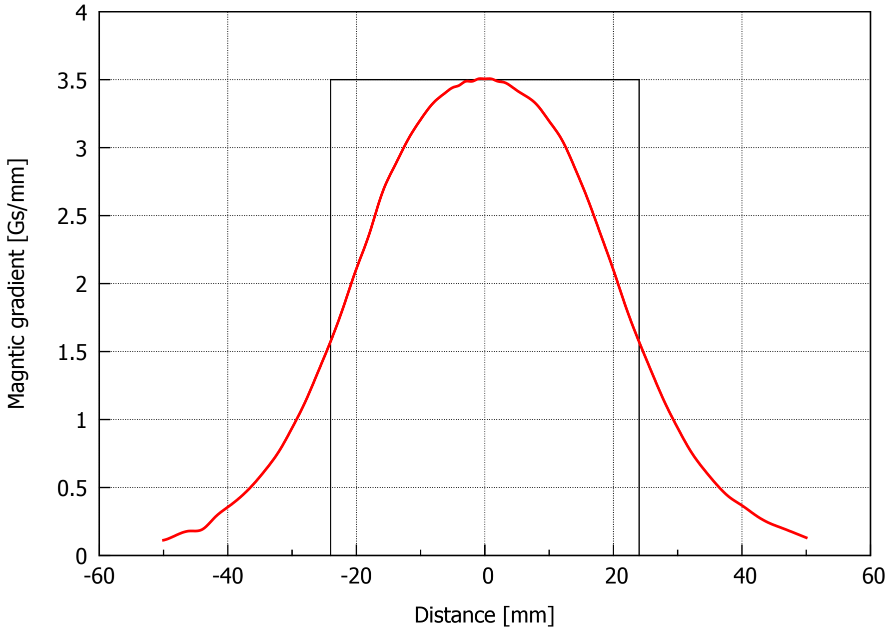

Figure 4.1.: The continuous gradient distribution representing the reference quadrupole, shown in red, for $I = 0.800\,\text{A}$. The black lines in the graph represent the hard-edge quadrupole with an effective length $l_{\text{eff}} = 0.048\,\text{m}$.

4.1.2. Investigating the Stability of the Transformation Matrix Elements

Before entering the overall transformation matrix parameters into the Beam Optic program, one must investigate the numerical stability of the overall transformation matrix . The following steps are taken to evaluate the numerical stability.

First, this gradient field distribution is divided equally into arbitrary numbers of 100, 200,... 900, and 1000 sections. Then, each time, after obtaining the individual transformation matrix, the overall transformation matrix is determined by multiplying the individual matrices, as it is stated in equation (2.22). Finally, by plotting the results of the overall transformation matrix elements as a function of the number of the small sections, which the gradient distribution is being divided into, we can investigate the numerical stability.

In Fig. 4.2 the variations of the transformation matrix element T_{21} is displayed.

As we had mentioned earlier, the element T_{21} determines the focal length of the quadrupole through the equality of $T_{21} = -\frac{1}{f}$.

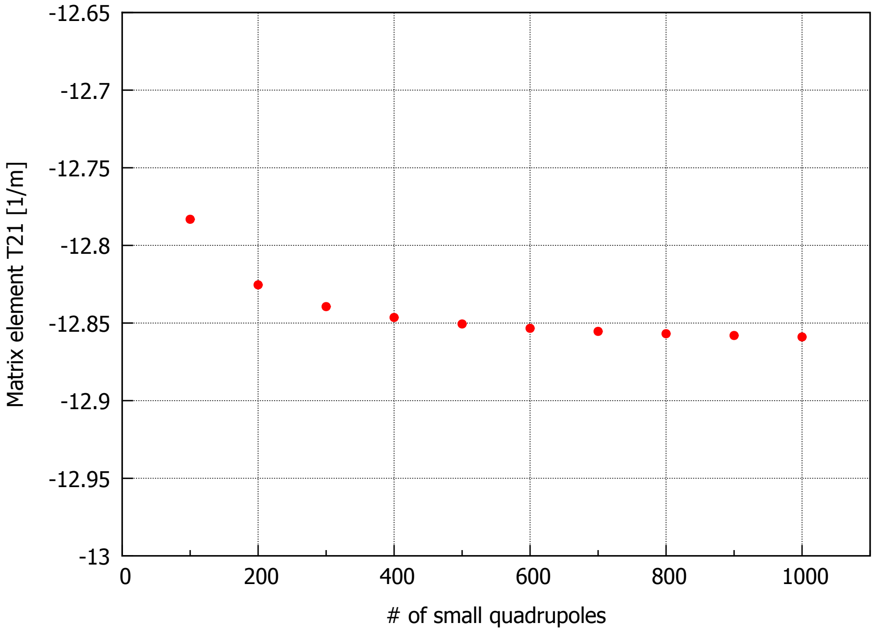

Figure 4.2.: The overall transformation matrix elements T_{21} as a function of the number of the small sections for $I = 0.800\,\mathrm{A}$

The result of these calculations for the transformation matrix elements T_{11}, T_{22} are put together in one graph, since the values of the elements are very close to each other. This result can be seen in Fig. 4.3. Finally, in Fig. 4.4 the result of the variations of the transformation matrix element T_{12} is displayed.

It is important to note that in obtaining these three graphs, we have used different resolutions. The graph for the two elements T_{11} and T_{22}, Fig. 4.3, has a resolution 10 times more than the graph for the element T_{21}, while the resolution of the graph for the T_{12} element, Fig. 4.4, is 1000 times more.

As these three graphs indicate, as we divide the quadrupole into more sections the value of the transformation matrix elements, at first, changes. Below a certain number of sections, around 600 sections, the numerical values are not stable. We assume the numerical stability of the transformation matrix elements start in the region when the field gradient distribution is being divided into at least 600 small sections and continues with a plateau. Therefore, for the remainder of our research to obtain the overall transformation matrix, we chose to divide the field gradient distribution into 800 small sections, since the division of the gradient distribution to 800 falls in the middle of the plateau.

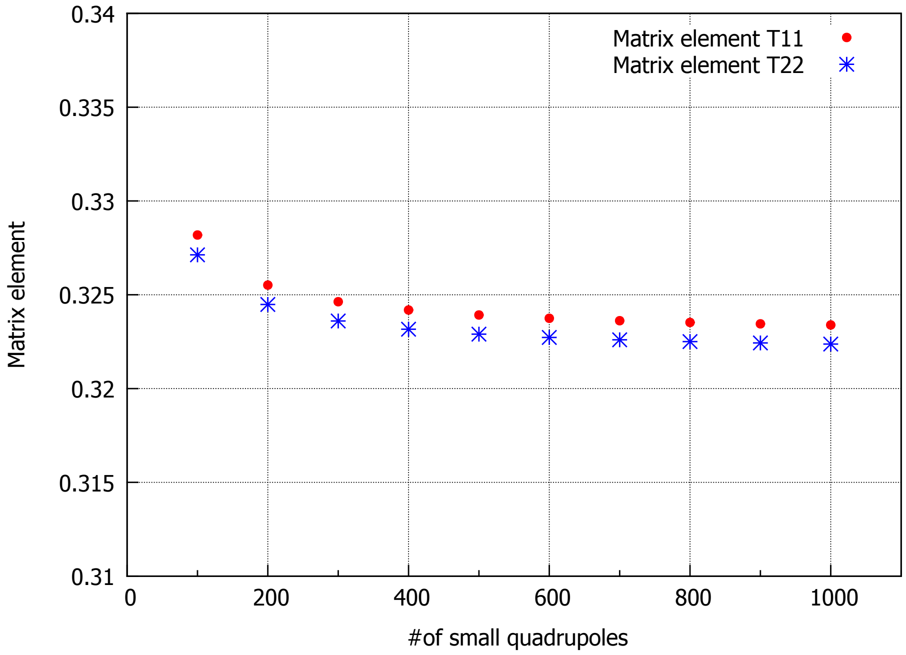

Figure 4.3.: The variations of the overall transformation matrix elements T_{11} and T_{22} in terms of the number of the small sections for$I = 0.800\,\mathrm{A}$

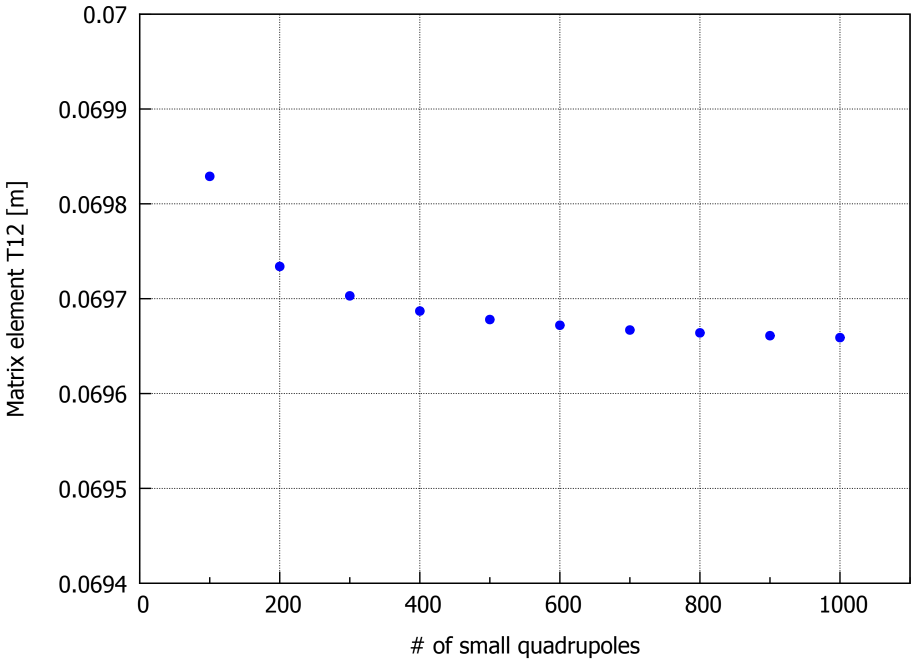

Figure 4.4.: The overall transformation matrix elements T_{12} as a function of the number of the small sections for $I = 0.800\,\mathrm{A}$

4.1.3. Finding the Best Focused Beam Size Using the Overall Transformation Matrix

Note that all the overall transformation matrices we have found so far are for the current $I = 0.8\,\text{A}$. Now, continuing with the same procedure as we change the current in increments of $I = 0.1\,\text{A}$, we will obtain the new magnetic strength, k, and therefore, the new gradient distribution.

Then, dividing the quadrupole gradient into 800 small sections, we will find the overall transformation matrix each time while changing the current from $I = 0.09\,\text{A}$ to $I = 0.27\,\text{A}$. Inserting the overall transformation matrix elements for the quadrupole parameters in the Beam Optic program, and using the same Twiss parameters for the source and the emittance as before —refer to equation (3.1)— we will measure the size of the beam.

The results of the variation of the beam size as a function of the current, as we divide the magnetic field gradient distribution into 800 small sections and find the overall transformation matrix, are illustrated with blue triangles in Fig. 4.5. For a quick comparison with the result of the hard-edge approach, from the previous chapter, the beam size as a function of the current for the hard-edge model is presented in red circles in the Fig. 4.5 as well. Also, the numeric values for the beam size for different currents are presented in Appendix A.2.

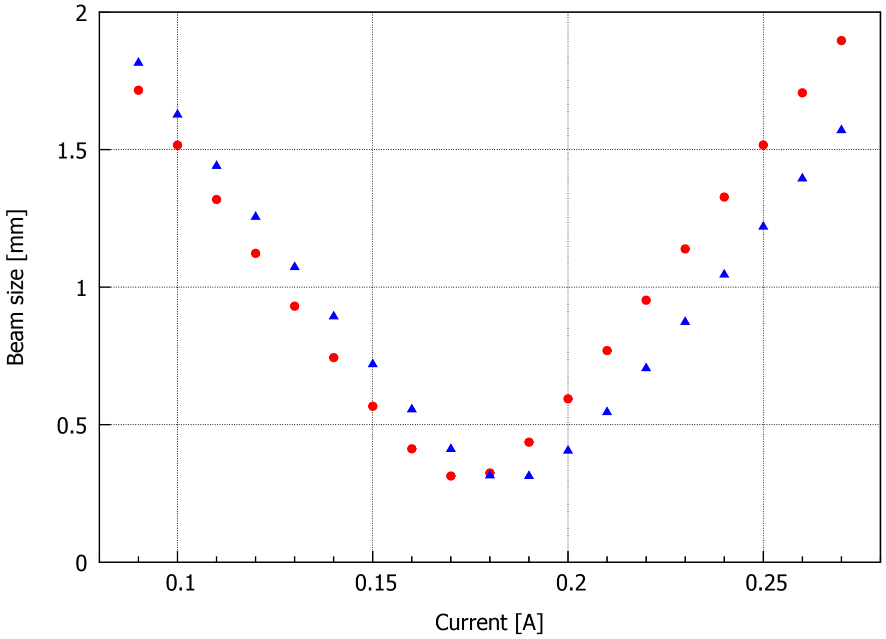

Figure 4.5.: Beam size as a function of current based on the overall transformation matrix of a quadruple (blue). Red circles demonstrates the beam size for the hard-edge model.

As it can clearly be seen from the Fig. 4.5, for the approach of finding the overall transformation matrix, the best focused beam occurs at about $I = 0.19\,\mathrm{A}$, as compared to the current $I = 0.17\,\mathrm{A}$ for the hard-edge model.

However, by considering the systematic error for the magnetic field gradient, which is about 5 %, we will observe that the curve for the hard-edge model would actually shift to the right. This shift for the $I = 0.17\,\mathrm{A}$ is almost 11 %. This , in turn, will result the point of the minimum to shift to almost $I = 0.17\,\mathrm{A}$, which is the minimum of the overall transformation matrix curve.

This is an indication that perhaps the large systematic error has caused the discrepancy between the hard-edge model and the overall transformation matrix method.

4.2. Comparing the Theoretical and Experimental Values

So far, in our two research approaches, which are explained both in the previous chapter as well as in this chapter, we have been able to find the current for obtaining the best focused beam theoretically and merely based on the two different computer simulations through the Beam Optic program.

Next, experimentally, in the PKAT beam line system, we allow the beam to only go through the quadrupole 3 by turning off all other beam line elements except quadrupole 3. Then, through a digital camera which is set in front of the screen, as it is shown in Fig. 3.9, we observe the beam on the screen next to the quadrupole 3.

The beam could be focused, in the focusing plane of the quadrupole 3, by changing of the control knobs for the quadrupole 3, located in the control room of the PKAT transport system, which as a result will change the quadrupole focal length. As we control the knobs, through the camera, we observe the size of the beam on the screen until it reaches the minimum size, and are able to take a picture of the real beam at the time of being focused. Fig. 4.6 displays a copy of the best focused beam created by using only the quadrupole 3 in the PKAT beam line system.

At this setting, the current going through the quadrupole 3 is measured directly by using a flux meter. We repeat this two times, the measured values for the current at the time of having minimum beam are

$I = 0.19\,\mathrm{A}$ and $I = 0.187\,\mathrm{A}$, averaging

$$I_{\mathrm{avg}} = (0.19 \pm 0.01)\,\mathrm{A} \tag{4.1}$$

4.3. True Quadrupole Effective Parameters

Since the current to achieve the best focused beam by using the method of dividing the gradient distribution into small sections and finding the overall transformation matrix has produced results that are in closer agreement with the actual experimental values, we would like to use the results of this approach and find out with what hard-edge quadrupole this gradient distribution could be replaced.

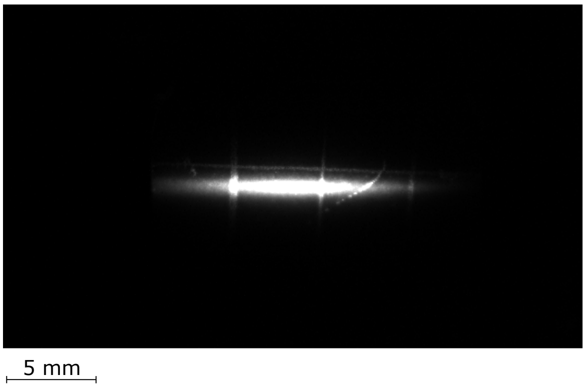

Figure 4.6.: The beam at its minimum size created by using only the quadrupole 3 in the PKAT

Now that we were able to determine the overall transformation matrix for the quadrupole, in order to obtain the correct treatment for the quadrupole, we look for the transformation matrix which is characterized by the correct quadrupole effective length and strength of a hard-edge model.

Since we have the magnetic field values for a length of 10 cm, in order to describe this 10 cm long section in the beam line by a matrix program, one could, at the first attempt, just consider that this 10 cm length is being composed of a hard-edge quadrupole of effective length $l_{\text{eff}} = 0.048\,\text{m}$ and two equal drift spaces of length $\lambda = 0.026\,\text{m}$ on each side, as it was illustrated in Fig. 2.2. In order to easily access and refer to that drawing, we have decided to present the picture once again.

The transformation matrix for such a system is found by Equation (2.25) in Chapter 2. Just as an example, for $I = 0.800\,\text{A}$ we have, $k = 312.36\,\frac{1}{\text{m}^2}$, resulting in $\varphi = 0.848$. Then, by plugging the values for l_{eff}, k, λ, and φ in the Equation (2.25), the matrix representation for the hard-edge model will be

$$T_{\text{Hardedge}} = \begin{pmatrix} 0.317 & 0.068 \\ -13.258 & 0.317 \end{pmatrix} \tag{4.2}$$

Now, to include the treatment for the end field fringes, we assume, as it was described in chapter 2, that this quadrupole gradient could be replaced with a hard-edge quadrupole of effective length l^+, and two drift spaces of equal length λ on each side.

Our attempt is to find the values of l^+, the true effective length of the quadrupole, and the true effective quadrupole strength, k^+, of this hard-edge representation of the real quadrupole. Recalling the equations (2.26) and (2.27) for a focusing quadrupole also, using the matrix elements we have found for dividing the gradient distribution into 800 small sections for $I = 0.800\,\text{A}$ and furthermore, applying the

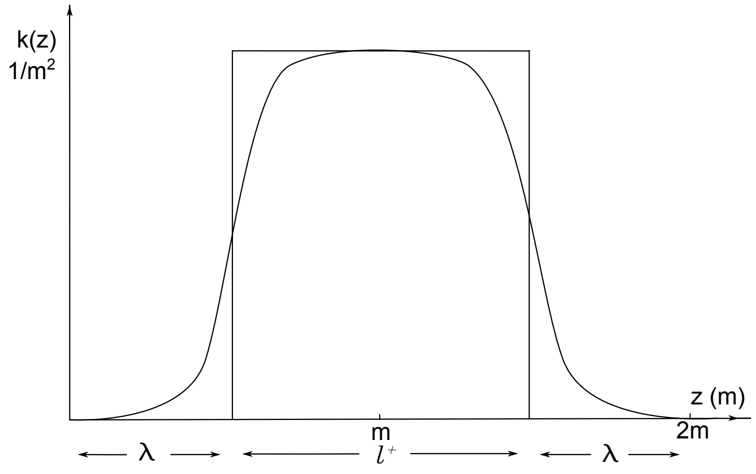

Figure 4.7.: Replacing the magnetic field profile with a hard-edge quadrupole

equality $2m = l^+ + 2\lambda$, where in our case, $2m = 10\,\text{cm}$, by using "Mathematica" and solving the equation (2.26) numerically, we will obtain

$$\varphi^+ = 0.963 \pm 0.009 \tag{4.3}$$

Inserting this value in the equation (2.27) , the effective length l^+ could be calculated:

$$l^+ = (0.061 \pm 0.001)\,\text{m} \tag{4.4}$$

Using the equality $\varphi^+ = \sqrt{k^+}l^+$ yields the actual quadrupole effective strength:

$$k^+ = (245.39 \pm 7.24)\,\frac{1}{\text{m}^2} \tag{4.5}$$

These true effective strength and length characterize the true matrix transformation for the 10 cm section of the beam line for $I = 0.800\,\text{A}$. The true transformation matrix could be written as

$$T_{\text{True}} = \begin{pmatrix} 0.323 & 0.070 \\ -12.857 & 0.323 \end{pmatrix} \tag{4.6}$$

It is important to recall the conventional values of the effective length and strength of a hard-edge quadrupole at $I = 0.800\,\text{A}$ and compare those values with the true quadrupole effective length and strength. In Table 4.1. these comparison is displayed.

The data in the Table 4.1 clearly shows that the true quadrupole effective length and strength are different from the customary definitions. Customarily, the quadrupole strength, k_0, is defined as the actual magnetic strength in the middle of the quadrupole and the magnetic length is measured to be $l_{\text{eff}} = 0.048\,\text{m}$ [21].

Table 4.1.: Comparing the quadrupole effective length and strength and associated driven functions for the two approaches for $I = 0.800\,\mathrm{A}$

	$l_{\mathrm{eff}}(\mathrm{m})$	$k\ (\frac{1}{\mathrm{m}^2})$	$\sqrt{k}l_{\mathrm{eff}}$	$\sqrt{k}\sin(\sqrt{k}l_{\mathrm{eff}})$
Conventional	0.048 ± 0.001	312.4 ± 0.1	0.84 ± 0.02	13.3 ± 0.2
True	0.061 ± 0.001	245.4 ± 7.2	0.96 ± 0.02	12.8 ± 0.3

The true quadrupole effective length is longer and the true effective strength is smaller than the conventional values of a pure hard-edge quadrupole. These deviations are 27.9 % and 21.4 % respectively for $I = 0.8\,\mathrm{A}$.

In order to better understand the difference between the true values and the conventional values of the quadrupole effective length and strength, these values, for $I = 0.800\,\mathrm{A}$, are put together in Fig. 4.8.

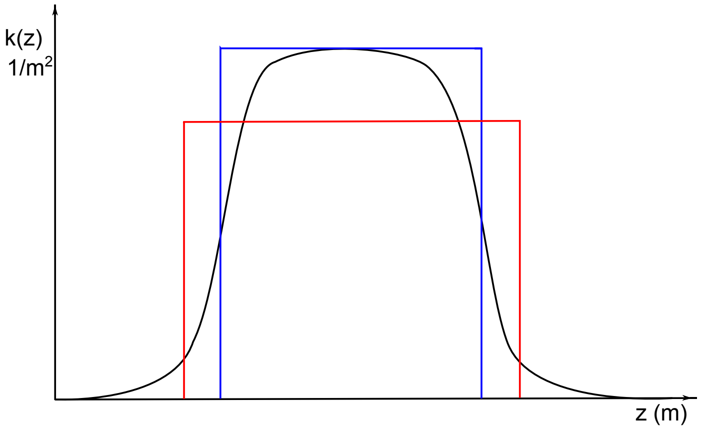

Figure 4.8.: Comparing the true (shown in Red) and conventional (in Blue) quadrupole strength and length for $I = 0.800\,\mathrm{A}$

Now, since we have proven that the true quadrupole effective length and strength are different from the customary definitions, it is worth, by using equation (2.30), to evaluate the relative deviations of the quadrupole parameters from the hard-edge model, and obtain the corrections needed for the quadrupole effective strength and length.

The relative field fringe corrections to the quadrupole strength and to the quadrupole length as a function of the magnetic strength k_0 are represented in Fig. 4.9. The calculated values of these deviations are shown in Appendix B.

As it could clearly be seen in Fig. 4.9, it is significant to factor in the fringe field corrections to the quadrupole effective strength and length in order to obtain more accurate results from the computer simulation program, otherwise, the result of the simulation would not be realistic.

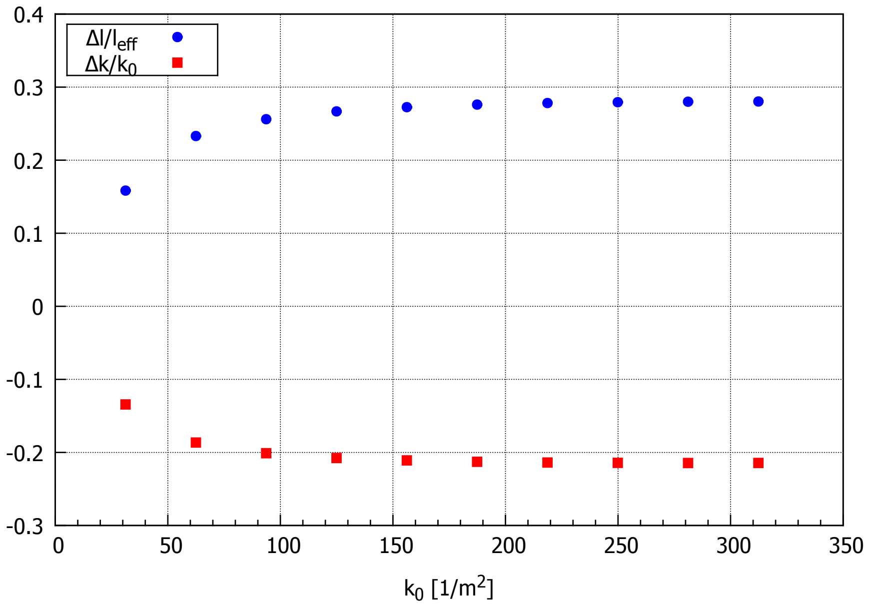

Figure 4.9.: The deviations of the effective length (blue) and the effective strength (red) of a hard-edge quadrupole

To include the deviations in the Beam Optic simulation, we must modify the program by entering the new values into matrices in the beam optic program. This might demand substantial computer programming effort, but would ensure the effectiveness of the simulation, which in turn guarantees a beam line configuration that could properly predict the behaviour of the electron beam, which therefore results in the design of the accelerator meeting specific goals.

Also, as we compare the transformation matrices T_{Hardedge} and T_{True} for $I = 0.800\,\text{A}$, obtainedin Equations (4.2) and (4.6), we observe that the deviation of the hard-edge matrix elements from the true transformation matrix are 1.9 % for the T_{11} and T_{22}, 11.7 % for T_{12}, and 3.1 % for T_{21}. This shows that these two matrices have comparatively small differences.

Therefore, although the deviations $\frac{(\Delta l)^+}{l_{\text{eff}}} = \frac{l^+ - l_{\text{eff}}}{l_{\text{eff}}}$ and $\frac{(\Delta k)^+}{k_0} = \frac{k^+ - k_0}{k_0}$, as it is illustrated in Fig. 4.9, seem considerably large, it is important to evaluate the deviation of $\Delta(k^+ l^+)$ from $k_0 l_{\text{eff}}$. These deviations are put together and presented in Appendix B.

It is interesting to note that the deviation of $\Delta(k^+ l^+)$ from $k_0 l_{\text{eff}}$ is actually small. This again proves that the actual differences for the matrix elements, between the hard-edge model and the method of the overall transformation matrix, will turn out to be small, at least for the lower quadrupole excitation. As an example, the relative deviation for the matrix element $T_{21} = \sqrt{k^+} \sin \varphi^+$ as a function of the current is calculated and shown in Fig. 4.10.

Based on this graph, we observe that the relative deviation of T_{21} varies only

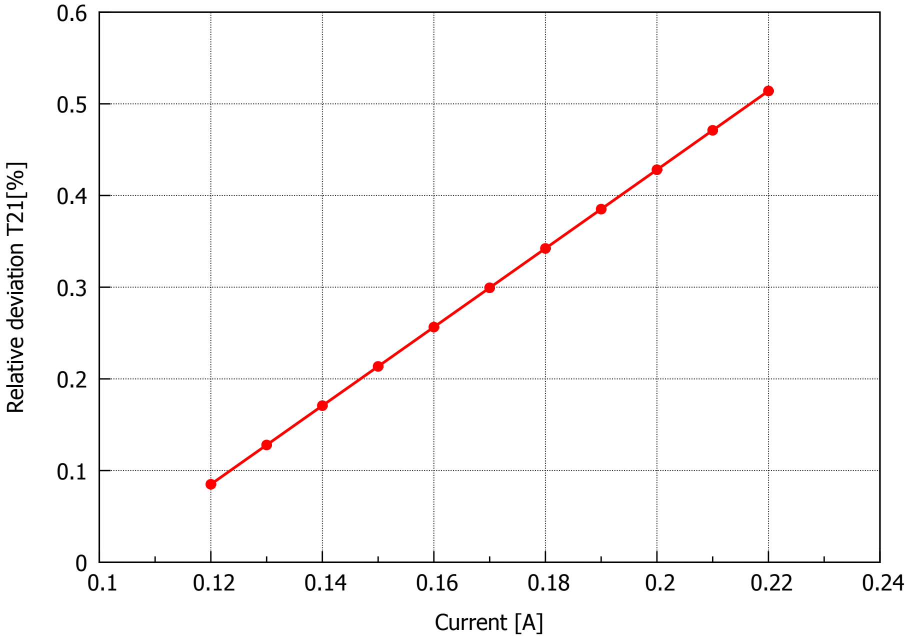

Figure 4.10.: The relative deviation of the matrix element T_{21} as a function of the current

by 0.3 to 0.5%, which is a good indication that the matrix elements would not be affected too much for the lower excitation between the two different approaches.

This rather small effect seem to support the observation in Fig. 4.5 and that the systematic error seem to lead to the shift between the hard-edge model and the overall transformation matrix method.

4.4. Correction due to the Extended Gradient

The magnetic gradient data points that we have used in our computer simulations do not extend to the point of $B = 0.0\,\mathrm{T}$ in either sides of the quadrupole,as can be seen in Fig. 4.1. Therefore, it is appropriate to consider the correction due to the remaining end-fields on both sides of the quadrupole.

In order to do that first, since based on the result of the overall transformation matrix approach the current at which we have the most focused beam occurs at $I = 0.19\,\mathrm{A}$, we choose to investigate this correction for $I = 0.19\,\mathrm{A}$. At this current, the overall transformation matrix, as we divide the gradient into 800 small sections will be

$$T = \begin{pmatrix} 0.826 & 0.092 \\ -3.447 & 0.825 \end{pmatrix} \tag{4.7}$$

Second, we will extend the gradient data, with arbitrary but realistic, data points for a 10 mm distance on each side of the original data points. Therefore, the magnetic field smoothly and neither linearly nor exponentially, will reach the zero point. A picture of this new extended gradient is demonstrated in Fig 4.11.

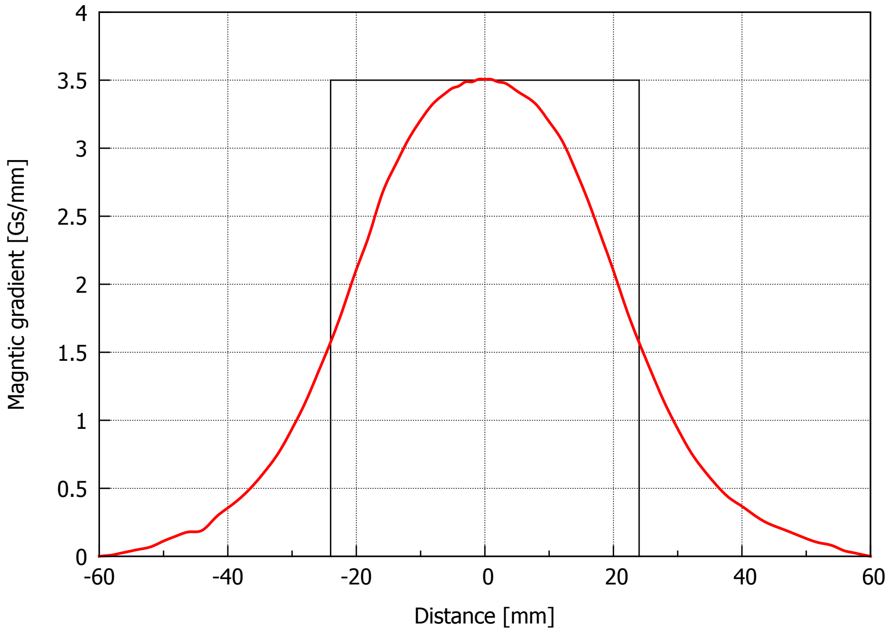

Figure 4.11.: The extended magnetic gradient distribution for the quadrupole, shown in red, for $I = 0.800\,\mathrm{A}$. The black lines in the graph represent the hard-edge quadrupole with an effective length $l_{\mathrm{eff}} = 0.048\,\mathrm{m}$.

The new overall transformation matrix for this extended gradient, as we again divide it into 800 small sections, for $I = 0.19\,\mathrm{A}$ will be

$$T_{\mathrm{extended}} = \begin{pmatrix} 0.853 & 0.093 \\ -2.921 & 0.853 \end{pmatrix} \tag{4.8}$$

Since we have extended the gradient data points for 10 mm on each side, this T_{extended} is for the total of 120 mm distance. Therefore, to be able to compare this extended overall transformation matrix with the transformation matrix from before, i.e. Equation (4.7), one must multiply the matrix in Equation (4.7) with a 10 mm drift space on each side. Doing so one will obtain

$$T_{\mathrm{original}} = \begin{pmatrix} 0.791 & 0.109 \\ -3.447 & 0.791 \end{pmatrix} \tag{4.9}$$

we name this transformation matrix T_{original} to distinguish between this transformation matrix and the one we found after making the necessary correction due to extending the magnetic gradient.

As we compare the matrix elements of T_{original} with T_{extended}, we observe that the deviations of the transformation matrix with the extended data are 3.3 % for the

T_{11} and T_{22}, 1.0 % for T_{12}, and 15.3 % for T_{21}. The fact that these deviations are not very small is another indication of the importance of considering the end-field effect completely and having full gradient data points before using the computer simulation.

5. Quadrupole Doublet

So far we have been able to study the behaviour of a single quadrupole and compare the two different approaches: The hard-edge model and the approach of the overall transformation matrix for the quadrupole gradient distribution. Since in any accelerator beam line there are more quadrupole doublets being used than just a single quadrupole, it seems appropriate to investigate the behaviour of the doublet in the accelerator beam line system.

In this chapter, we use the same strategy of treating a single quadrupole, as it was described in Chapters 3 and 4, and apply it to the first quadrupole doublet in the PKAT beam line transport system, i.e. quadrupoles 3 and 4.

For a quick reference, a close up picture of this quadrupole doublet in the PKAT beam line is shown in Fig. 5.1.

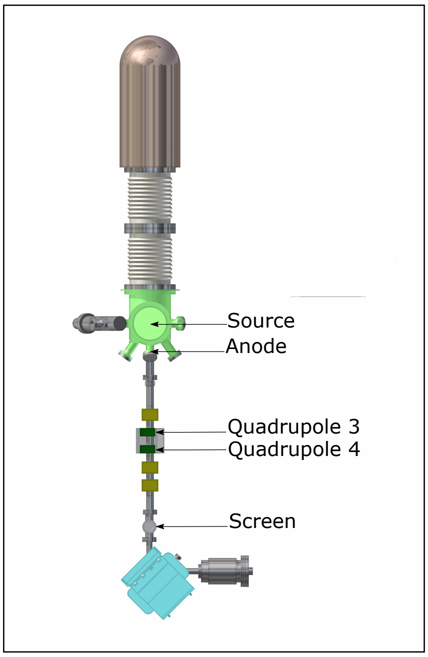

Figure 5.1.: The close up location of the source, anode, quadrupole doublet, and the screen in the PKAT beam transport system

After finding the quadrupole parameters for both quadrupoles, these parameters are entered in the Beam Optic simulation program. Then, the current to achieve the most focused beam through the quadrupole doublet is obtained. In doing so, we use the two approaches of the hard-edge quadrupoles and the overall transformation matrix. Finally, at the end of the chapter, we compare the theoretical and experimental values of the current to attain the best focused beam.

Recalling the measurements that were presented in Chapter 3, in Table 2 and Fig. 3.6, we observe that the quadrupoles 3 and 4 have different resistance and show very different magnetic field behaviour. These quadrupoles have the same geometrical length (41 mm), and are separated by a drift space of 42 mm.

However, since quadrupole 3 and 4 are being used together as a quadrupole doublet in the beam line, their polarities must be opposite of each other. This means if one is focusing in one plane then the other one must be defocusing in that same plane. Furthermore, we assume that the magnetic field gradient distribution of both of these quadrupoles are equal in magnitude.

5.1. Hard-Edge Model

In the first part of this chapter we, again, consider both of these quadrupoles as hard-edge quadrupoles with having similar magnetic field. For the time being, we also, assume that these quadrupoles have the same magnetic field gradient, We will include the affect of the difference in their resistance later. We will use the Beam Optic computer simulation program and enter the parameters for the source and each of these quadrupole doublet in the program.

The Twiss parameters for the source, the values of the emittance, and the effective length of the quadrupole $l_{\text{eff}} = 48\,\text{mm}$ are as before, refer to Section 3.1. The distance from the source to the quadrupole 3 (Drift 1) was obtained in Section 3.2. By measuring the drift space in between the two quadrupole doublets (Drift 2) and also from the quadrupole 4 to the screen (Drift 3) we will have

$$\alpha = -1.05 \qquad , \qquad \beta = 0.23\,\frac{\text{mm}}{\text{mrad}} \qquad , \qquad \gamma = 9.31\,\frac{\text{mrad}}{\text{mm}} \tag{5.1}$$

$$\text{Drift1} = 46.85\,\text{cm} \quad \text{and} \quad \text{Drift2} = 3.50\,\text{cm} \quad \text{and} \quad \text{Drift3} = 45.75\,\text{cm} \tag{5.2}$$

5.1.1. Horizontal and Vertical Planes

Following the same approach as we introduced in section 3.2 for a single quadrupole, in order to use the Beam Optic simulation program for the quadrupole, we need to have the quadrupole magnetic strength for each of these quadrupoles for a specific current. We assume that the quadrupole 3 is focusing in the horizontal plane and therefore, quadrupole 4 is defocusing. The magnetic field gradient of quadrupole 3 was measured (Equation 3.2) as

$$g_3 = 4.63\,\frac{\text{mT}}{\text{cm}} \tag{5.3}$$

The quadrupole strength of this quadrupole, for different currents, was determined by using the equation $k = \frac{e}{p}g$.

To obtain the magnetic field strength of the quadrupole 4, we will use the fact that the quadrupole 4 is being used along with the quadrupole 3 as a quadrupole doublet. We assume therefore, that the magnetic gradient, and as a result, the magnetic field strength of the quadrupole 4 must be equal but with opposite polarity to that of quadrupole 3.

$$g_4 = -4.63\,\frac{\mathrm{mT}}{\mathrm{cm}} \tag{5.4}$$

Then, in principle, by having the magnetic strength of quadrupole 4 for each current, after entering these parameters into the Beam Optic program, the size of the beam could be obtained. Next, by changing the current and repeating the same steps, we determine the variation of the beam size in terms of the current for this quadrupole doublet.

We will consider the result of this hard-edge model in two planes. First, in the horizontal plane, assuming that the quadrupole 3 is focusing in the (x, z) plane and that the quadrupole 4 is defocusing and then, in the vertical plane, by reversing the polarities of each of these quadrupole doublet. These results are illustrated in Fig. 5.2. In this graph, the red circles and the blue triangles represent the size of the beam as a function of the current in the horizontal and the vertical planes respectively.

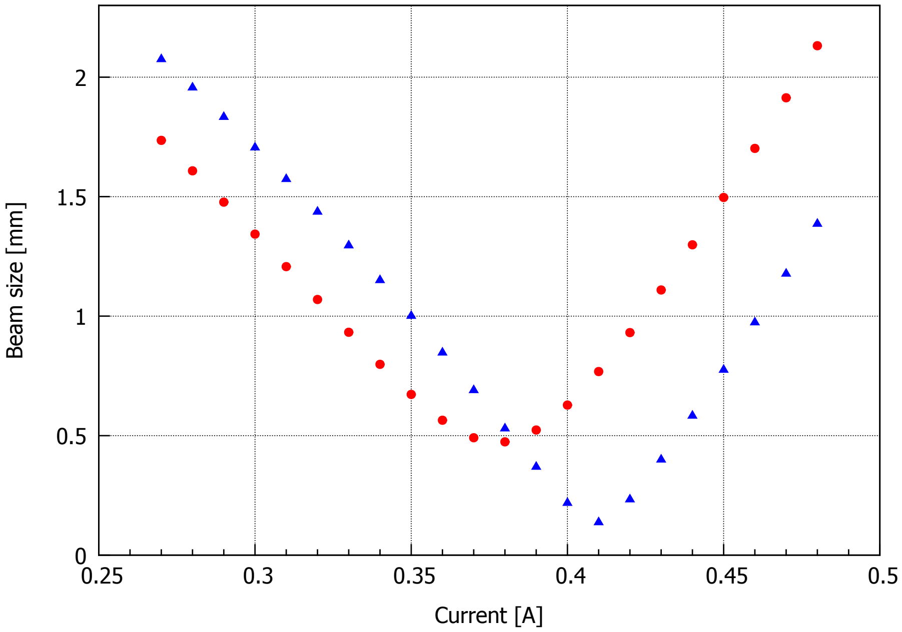

Figure 5.2.: The size of the beam for the quadrupole doublet as a function of the current in the horizontal (red) and vertical (blue) planes using the hard-edge model

The obtained values for the beam size from the Beam Optic simulation program, for the hard-edge quadrupole doublet, are put together in the Appendix C.1.

5.1.2. Both Planes

In order to investigate the current that would produce the best focused beam, as the current goes through the hard-edge quadrupole doublet, we use the values that we have obtained for the beam size in both the horizontal and the vertical plane and take the following steps.

First, for each of the currents, by looking at the size of the beam in the x and the y planes —refer to Appendix C.1— we take the maximum values between the size of the beam in the x and the y plane. Then, we observe how these values are changing with the current. The variations of these maximum values as a function of the current are being plotted in the Fig. 5.3.

These maximum values reach a minimum, as it is seen in Fig. 5.3. Finally, we take the minimum of all these maximums. The current associated with that represents the current to achieve the most focused beam for the hard-edge representation of the quadrupole doublet based on the Beam Optic simulation.

As Fig. 5.3 indicates, for the quadrupole doublet using the hard-edge model, the current to obtain the best focused beam occurs at about $I = 0.39\,\mathrm{A}$.

Later on, at the end of this chapter, after finding the current to achieve the most focused beam using the overall transformation matrix approach, we will compare this value with the experimental value of the current to achieve the best focused beam for this quadrupole doublet in the PKAT transport system.

5.2. Overall Transformation Matrix

In this part of our research, our goal is to include the improved treatment of the quadrupole end field effect for both quadrupole 3 and 4, as it was described in section 4.2, and find the current to achieve the most focused beam. We, again, use the same gradient distribution [23] for the 10 cm that we have used for the single quadrupole, and use the continuous magnetic field distribution obtained by using the Spline program.

Fig. 5.4 demonstrates the magnetic distribution for the quadrupole doublet, shown in red. The outline of the quadrupole doublet, with $l_{\text{eff}} = 0.048\,\mathrm{m}$, is shown with the black lines in the graph.

It must be noted that since the original magnetic field gradient data had a small asymmetry as respect to the symmetry line of the quadrupole, as we had mentioned in section 4.1.1, as a result in Fig. 5.4 the curve in the area in between the two quadrupoles is not smooth.

Following the steps with the quadrupole singlet, we choose to divide the magnetic field gradient of each of the quadrupole doublet into 800 small sections and find the overall transformation matrix for quadrupole 3 and 4.

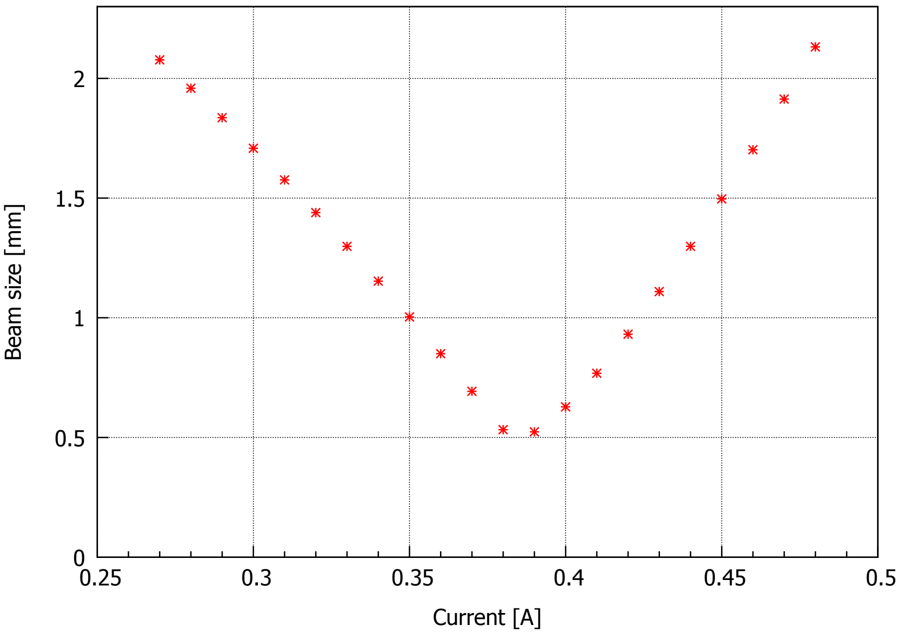

Figure 5.3.: The size of the beam for the hard-edge quadrupole doublet as a function of the current in both planes

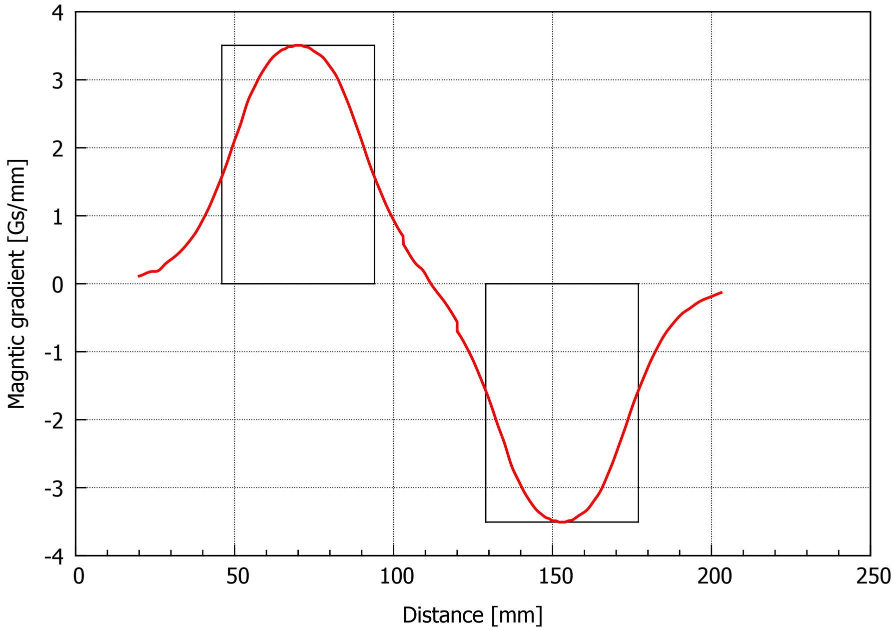

Figure 5.4.: The continuous gradient distribution, shown in red, for the quadrupole doublet for $I = 0.800\,\mathrm{A}$. The black lines represent the hard-edge quadrupole doublet with the effective length $l_{\mathrm{eff}} = 0.048\,\mathrm{m}$.

Since the drift space in between these two quadrupoles is only 42.0 mm, these two 10 cm magnetic gradient distributions, which are equal in magnitude and have opposite polarity, overlap with each other and cover the entire drift space in between the quadrupole doublet. Therefore, in finding the total overall transformation matrix for the quadrupole doublet, which is done by using the "Octave" computer program, we must consider the region of their overlap.

Since the magnetic field gradient distributions for the quadrupole doublet overlap and cover the entire existing drift space in between the two quadrupoles, we simply do not need to consider that drift space in our simulations. After making the necessary adjustments for the drift spaces, from the source to the beginning of the magnetic gradient distribution of quadrupole 3 (Drift 1) and from the end of the gradient distribution of quadrupole 4 to the screen (Drift 2), this will result in

$$\mathrm{Drift1} = 44.25\,\mathrm{cm} \quad \text{and} \quad \mathrm{Drift2} = 43.15\,\mathrm{cm} \tag{5.5}$$

Then, the values of the drift spaces, total transformation matrix elements for the system of the quadrupole doublet, parameters for the source, and the values for the emittance are entered into the Beam Optic program to find the size of the beam.

5.2.1. Horizontal and Vertical Planes

Following the steps that are mentioned, in applying the improved treatment of the quadrupoles end-effect for the quadrupole doublet under study, and in obtaining the overall transformation matrix for the system of the quadrupole doublet, we consider their behaviour in both the horizontal and vertical planes.

In the horizontal plane, we assume, as it was the case in the hard-edge model approach, that the quadrupole 3 is focusing and as a result, quadrupole 4 is defocusing. In the vertical plane, the polarity of these doublet is switched, which simply means their magnetic gradient distributions are reversed. After using the Octave program and calculating the overall transformation matrix for the doublet in both planes, the quadrupole parameters could be entered in the Beam Optic simulation.

It must be noted that the values of the overall transformation matrix in the horizontal plane must be inserted in the horizontal plane of the Beam Optic program. Each of the four elements obtained in the calculation of the overall transformation matrix must be entered for the elements R_{11}, R_{12}, R_{21}, and R_{22} respectively. Similarly, the overall transformation matrix elements for the vertical plane must be entered in place of the the elements R_{33}, R_{34}, R_{43}, and R_{44} of the Beam Optic program respectively.

Finally, by changing the current, which changes the gradient distributions and therefore changes the overall transformation matrices, we can observe how the size of the beam changes. Fig. 5.5 represents the size of the beam as a function of the current for the horizontal and the vertical planes.

In Appendix D, the obtained values for the size of the beam for different currents using the overall transformation matrix approach for the quadrupole doublet are listed.

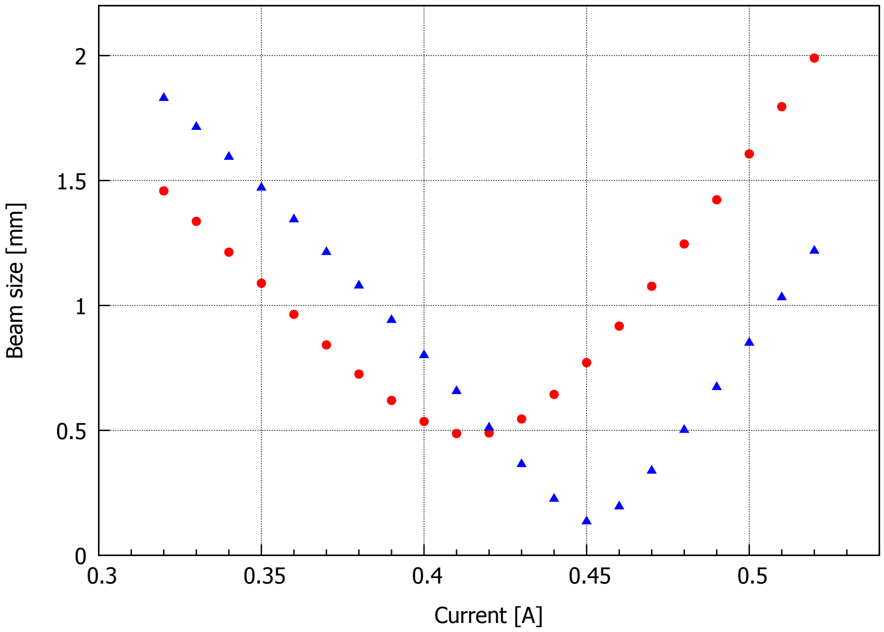

Figure 5.5.: The size of the beam for the quadrupole doublet as a function of the current in the horizontal (red circles) and vertical planes (blue triangles) using the overall transformation matrix

5.2.2. Both Planes

To study the behaviour of the quadrupole doublet while applying the overall transformation matrix approach, and be able to obtain the current of achieving the most focused beam, we follow the same procedure as we did for the hard-edge model which was discussed in section 5.2.1. The maximum values of the size of the beam in each plane as a function of the current, which are taken from Appendix D, are plotted and illustrated in Fig. 5.6.

The current at which these maximums come to a minimum represents the current that produces the best focused beam for the quadrupole doublet using the overall transformation matrix method. As Fig. 5.6 indicates, for this model, the current to achieve the most focused beam for the quadrupole doublet happens at about $I = 0.42\,\mathrm{A}$.

5.3. Comparing the Theoretical and Experimental Values

So far in this part of our research, we have determined the current to obtain the most focused beam by applying the two different approaches and using the Beam Optic computer simulation program. In order to obtain the current for the most focused beam experimentally, the same set-up as it was mentioned in section 4.3 has been used. In the PKAT beam line transport system, a digital camera is set in front

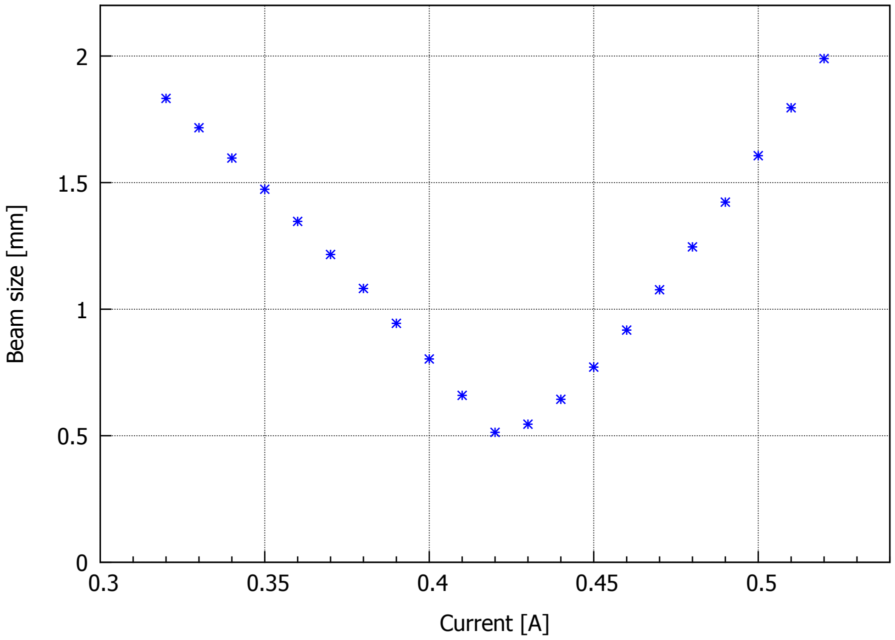

Figure 5.6.: The size of the beam for the quadrupole doublet as a function of the current in both planes using the overall transformation matrix

of the screen which is located right after the quadrupole 4, as it is shown in Fig. 5.1.

Then, by turning off all the other elements except quadrupole doublet 3 and 4, we allow the beam to only go through this quadrupole doublet. Next, by changing of the control knobs in the PKAT for these two quadrupoles, which changes their quadrupole focal length, we, through the digital camera, observe how the size of the beam changes on the screen. As we continue changing the settings of the control knobs for these two quadrupoles, we observe the size of the beam until it is focused. Through the digital camera a picture of the beam, when it is focused the most, is taken and is displayed in Fig. 5.7.

Recalling the results we had obtained in both the hard-edge and the overall transformation matrix simulations for the quadrupole doublet, refer to the Fig. 5.2 and Fig. 5.5, the size of the beam seems to be different in the horizontal and vertical planes.

As the two graphs indicate, in both simulations, the size of the beam is smaller in the vertical plane as compared to the horizontal plane, by a factor of 3.4 % for the hard-edge model, and by a factor of 3.5 % for the overall transformation method. However, the beam when it is focused, as it is seen in the Fig. 5.7, seems round.

However, in the PKAT control room, after focusing the beam by the quadrupole doublet, we looked at the beam in the horizontal and the vertical plane separately. No significant difference was observed between the beam sizes in the horizontal and the vertical planes.

Figure 5.7.: The beam at its minimum size created by using the first quadrupole doublet in PKAT

At the setting of having the best focused beam through the quadrupole doublet, the current going through each of these two quadrupoles are measured. This measurement is obtained using a multimeter and by directly measuring the current going through each of these two quadrupoles on the back of the power supply. The experimental values for the current going through each of the quadrupole doublet 3 and 4 are respectively shown below.

$$\mathrm{I}_3 = (0.35 \pm 0.01)\,\mathrm{A} \quad \text{and} \quad \mathrm{I}_4 = (0.79 \pm 0.01)\,\mathrm{A} \tag{5.6}$$

We must note that, recalling the results from the Fig. 3.7, the magnetic field and therefore, the gradient for the quadrupole 3 and 4 has the ratio of $\frac{9.2}{4.1}$. Therefore, as we choose to use these two quadrupoles as a doublet, it is expected that the current which goes through each of them would be different and follow $\mathrm{I}_4 = \frac{9.2}{4.1}\mathrm{I}_3$, which is in agreement with the measured values in Equation 5.6.

As we compare the results of our two computer simulations for the doublet in obtaining the current for the best focused beam with the experimental values, we realize that, contrary to our expectations, it appears that the method of the overall transformation matrix did not produce the favourable results. However, we must mention the following factors that have contributed to this surprising outcome.

First and foremost, quadrupole 4 has demonstrated very strange behaviour. The design of the quadrupole 4 is very different than of quadrupole 3, and even of the remaining quadrupoles in the PKAT beam transport system. Different coils, with different windings have been used in the structure of the quadrupole 4. This, as a result, has caused that the magnetic gradient of the quadrupole 3 and 4 not to be the same even though they are used as a doublet.

In addition, as it is illustrated in Fig. 3.7, for the magnetic field of the quadrupole 3 we were able to have two measurements averaging at $B = 9.4\,\mathrm{mT}$. Due to the fact that we have grouped quadrupole 3 and the reference quadrupole in one group, we simply have used the gradient of the reference quadrupole in place of the gradient of the quadrupole 3. By doing so, we have ignored the 2.2 % error between the average magnetic field of the quadrupole 3 and the reference quadrupole. This error could be 5.3 % at the highest if one considers the greater measured value of the magnetic field for quadrupole 3.

But for quadrupole 4, since due to the lack of accessibility, we were able to make only one measurement, we had used the ratio of its magnetic field to the magnetic field of the reference quadrupole, i.e. $\mathrm{B}_4 = \frac{4.1}{9.2}\mathrm{B}_3$.

In overall, there seem to be a large systematic error in the magnetic field strength of the quadrupole 4 creating this surprising large discrepancy.

6. Conclusion

In preparation for the construction of MESA and also for the time resolved measurements, the purpose of our research has been to study the behaviour of the large aperture quadrupoles in the PKAT transport system. In achieving that goal our focus has been on which current would yield the most focused beam based on the computer simulation, and compare it to the experimental value.

By using the Beam Optic computer simulation program, we have implemented two different approaches. First, using only the hard-edge model for a quadrupole. Then, we have applied the improved treatment of the quadrupole end-effect and obtained the quadrupole overall transformation matrix. We have applied these methods to a single quadrupole and then, have extended it to the quadrupole doublet.

For the single quadrupole, as we compare the results of the simulation with the experimental value we see that the customary definitions of the quadrupole effective length and strength, from a hard-edge model for quadrupoles are ineffective in reality. If we merely consider the customary definitions the discrepancy between the two values of the current is almost 12 %.

As we included the improved treatment of the end field fringes into our simulations by calculating the overall transformation matrix, we see that the values of the current to achieve the most focused beam are in much better agreement with each other, less than 0.1 %.

For the quadrupole doublet, as we compare the results of our two simulations with the experimental values of the current to obtain the best focused beam, we realize that the deviations from the experimental value are 8.6% and 17.1% for the hard-edge model and the method of the overall transformation matrix respectively.

This, unexpected and unfavourable, result could be due to the fact that the two quadrupoles do not have the same parameters. The geometric design, the thickness of the coils and the number of windings of them are different. The large error in accurately determining the magnetic field gradient of the quadrupole 4 has caused the large systematic error, creating such a surprising and large discrepancy between the computer simulation and the experiment.

It is also important to note that the corrections $\frac{(\Delta l)^{\pm}}{l}$ and $\frac{(\Delta k)^{\pm}}{k_0}$ are small for quadrupoles which have a small ratio of aperture to length. However, these corrections are larger for quadrupoles with a high ratio of aperture to length, as it is the case with the quadrupoles currently being used in PKAT and also the ones that will be used in the construction of MESA. Therefore, it is necessary to include these modifications to the conventional beam transport system. Depending on the excitation of such quadrupoles, a correction to the quadrupole effective length and strength needs to be considered.

7. Outlook

In our research, in obtaining the overall transformation matrix, we have used the magnetic field distribution of a quadrupole for a 10 cm distance, in which the magnetic field drops from its maximum value, in the middle of the quadrupole, to the values of $0.013\,\frac{\mathrm{T}}{\mathrm{m}}$ and $0.011\,\frac{\mathrm{T}}{\mathrm{m}}$ on either side of the quadrupole.

Although we investigated the correction to this problem by extending the magnetic gradient for 10 mm on each side, one modification to this project would be to actually measure the field gradient of the quadrupole for a longer distance outside of the quadrupole to the points where the magnetic field would indeed be zero.

As we have concluded, the behaviour of a quadrupole in a beam line system can be understood more accurately only if we include the quadrupole end-effect more accurately.

In our project the chosen quadrupole doublet consisted of two quadrupoles which were not similar and as a result had different parameters. To improve the result of our research, one could first, study the behaviour of a quadrupole doublet made of two similar quadrupoles, with similar design and gradient, and then compare the results of the theoretical and experimental values of the current to achieve the most focused beam. Also, one could actually measure the magnetic gradient of the quadrupole 4 in the PKAT beam transport system accurately, without assuming the ratio of their magnetic gradient, and therefore reduce the large systematic error.

Since there are a lot of triplet quadrupoles being used in the beam line of the accelerator systems, to further expand the scope of our research, one could use the same strategy of treating one quadrupole and apply it to a combination of three quadrupoles and find out how the transformation matrices of the combination of quadrupoles would affect each other and also the current to obtain the best focused beam.

To take this even one step higher, one could take this method of using the overall transformation matrix after dividing the gradient to small sections and apply it to all the quadrupoles present in the PKAT beam line system in order to have a better understanding of how the whole system of different combinations of the quadrupoles works and be able to compare the result of the computer simulation program with the reality.

And of course, as the steps are being taken in the process of constructing MESA, we could be sure of a more predictable and therefore more successful outcome for the operation of MESA, if we take into consideration the improved treatment of the quadrupole end-effect and use the overall transformation matrix method for each of the large aperture quadrupoles planned to be used in the construction of MESA beam line.

A careful application of the overall transformation matrix for each of these basic building blocks of MESA, the quadrupoles, would allow a more accurate design of the beam line, which provides a more effective operation, which in turn will result in the construction of MESA meeting the specific goals, for which it is proposed. In addition, it would provide the necessary information required in preparing and performing the time resolved polarization measurements by using the spin rotator Wien filter.

Acknowledgement

This research has been accomplished with the help of many. It has been a great opportunity for which I thank God for providing it for me and also enabling me to accomplish it.

I would like to express my appreciation to all those who have contributed, in many ways, to the accomplishment of this research.

Most of all, I would like to thank Professor Dr. Aulenbacher for granting me the opportunity to pursue this research. I truly appreciate his support and encouragements, along with providing countless guidance and suggestions during my research, when I needed them.

My sincere thanks go to all my colleagues in the B2 group. I appreciate all their friendship, support, and help. However, I would like to, particularly, recognize just a few of them and their great contributions:

I specially am grateful to Simon Friederich for much help with the computer programs, to Tobias Weilbach for his instructions and help with the PKAT lab, to Daniel Simon regarding the Beam Optic program, and to Max Bruker for his help throughout my research and specially in revising my thesis.

My special thanks go to Dr. Valerie Tioukine, and my colleagues Steffen Heidrich and Christoph Matejcek for assisting me in different areas throughout my time working on my project.

I also would like to express my heartfelt appreciation to my dear Mom, and all my sisters and brothers, for their love and encouragements all along, even though we have been physically far apart.

And last but not least, I am most grateful to my loving husband, Michael, and my wonderful boys, Michael, Daniel, Andrew, and Joshua for their incredible and unmeasurable love, support, understanding, encouragements, and all the sacrifices they have made throughout my research. Truly, without each and everyone of their help and support the completion of this project would have been impossible.

Bibliography

[1] D. Becker · S. Baunack · F. E. Maas, P2—a new measurement of the weak charge of the proton, Springer Science+Business Media Dordrecht, 2013

[2] F. Schlander, K. Aulenbacher, et al.: Investigation of cryomodules for the Mainz energy-recovering Superconducting Accelerator MESA. In: Proc. IPAC2014, Dresden (2014), pp. 2505–2507

[3] R. Heine, et al. Lattice And Start To End Simulation of the Mainz Energy Recovering Superconducting Accelerator MESA. In: Proceedings of the 2012 International Particle Accelerator Conference (IPAC 2014). 2014.

[4] K. Aulenbacher, et al. Status of the MESA accelerator. In: Proc. ERL2013, Novosibirsk, Russia (2013), pp. 1–5

[5] R. Heine, K. Aulenbacher, R. Eichhorn: MESA-Sketch of an energy recovery linac for nuclear physics experiments at Mainz. In: Proc. IPAC2012, New Orleans (2012), pp. 1993–1995

[6] K. Aulenbacher, Opportunities for parity violating electron scattering experiments at the planned MESA facility, Springer Science+Business Media B. V. pp. 3–7 (2011)

[7] T. Maruyama, et al.: Systematic study of polarized electron emission from strained GaAs/GaAsP superlattice photocathodes. Appl. Phys. Lett. 85, 2640 (2004)

[8] K. Aulenbacher, et al., Journal of Applied Physics, Vol. 92, No.12 (2002)

[9] J. Hubner, M. Oestreich, Springer Series in Solid-State Sciences Volume 157, (2008), pp. 115–134

[10] L. G. Gerchikov, et al., Journal of Physics: Conference Series 298 (2011) 012013

[11] K. Aulenbacher, Eur. Phys. J. Special Topics 198, 361–380 (2011)

[12] K. Aulenbacher, et al. Nucl. Instr. and Meth. in Phys. Res. A 391(1997) 498–506

[13] V. Tioukine, K. Aulenbacher, Nucl. Instr. and Meth. in Phys. Res. A 568 (2006) 537–542

[14] K. Wille, The Physics of Particle Acceleratoes, Oxford University Press Inc., New York, 2005

[15] H. Wiedemann, Particle Accelerator Physics, Springer-Verlag, Berlin, 2007

[16] K. G. Steffen, High energy beam Optics. Wiley, New York, 1965

[17] V. Bargmann, L. Michel, and V. L. Telegdi, Phys. Rev. Lett.2, 435 (1959)

[18] S. Penner, Calculations of properties of magnetic deflection systems. The review of scientific Ins., Vol. 32, No.2 (1960)

[19] M. Salomaa; H. A. Enge, Velocity selector for heavy-ion separation. Nucl. Instr. and Meth. 145 (1977)

[20] K. Aulenbacher, Eine Quelle longitudinalpolarisierter Elektronen Fur das MAMI-Beschleunigersystem, Institute fur Physik, JGU, 1993

[21] K. H. Steffens, Konzeption und Optimierung eines 100 keV Injektionssystems zur Erzeugung eines longitudinal polarisierten Elektronenstrahls am MAMI, Institute fur Kernphysik, JGU, 1993

[22] K. Aulenbacher, Erzeugung intensiver hochpolarisierter Elektronenstrahlen mit hoher Symmetrie unter Helizitatswechsel, Institute fur Kernphysik, JGU,2007

[23] S. Heidrich, Experimentelle Bestimmung von Quadrupolparametern an der Testquelle des Mainzer Mikrotrons, Institute fur Kernphysik, JGU, 2012

Appendix A.

Tables of Data

A.1. Single Quadrupole, Hard-Edge

I(A)	Beam size (mm × mm)
0.10	1.5162 × 2.6818
0.11	1.3184 × 2.8087
0.12	1.1229 × 2.9361
0.13	0.9307 × 3.0641
0.14	0.7438 × 3.1927
0.15	0.5669 × 3.3218
0.16	0.4123 × 3.4514
0.17	0.3133 × 3.5815
0.18	0.3243 × 3.7120
0.19	0.4362 × 3.8431
0.20	0.5940 × 3.9747
0.21	0.7694 × 4.1067
0.22	0.9524 × 4.2391
0.23	1.1390 × 4.3721
0.24	1.3274 × 4.5054
0.25	1.5167 × 4.6392
0.26	1.7065 × 4.7735
0.27	1.8963 × 4.9082

A.2. Single Quadrupole, Overall Transformation Matrix

I(A)	Beam size (mm × mm)
0.09	1.8175×1.3841
0.10	1.6292×1.3841
0.11	1.4424×1.3841
0.12	1.2574×1.3841
0.13	1.0748×1.3841
0.14	0.8956×1.3841
0.15	0.7217×1.3841
0.16	0.5574×1.3841
0.17	0.4135×1.3841
0.18	0.3175×1.3841
0.19	0.3152×1.3841
0.20	0.4074×1.3841
0.21	0.5476×1.3841
0.22	0.7073×1.3841
0.23	0.8754×1.3841
0.24	1.0475×1.3841
0.25	1.2217×1.3841
0.26	1.3969×1.3841
0.27	1.5725×1.3841

Appendix B.

B.1. Field Fringe Deviations

$\frac{k}{k_0}$	$\frac{k^+ - k_0}{k_0}$	$\frac{l^+ - l_{\text{eff}}}{l_{\text{eff}}}$	$\frac{\Delta(k^+ l^+)}{k_0 l_{\text{eff}}}$
0.1	-0.1343	0.1584	0.0028
0.2	-0.1865	0.2331	0.0032
0.3	-0.2011	0.2561	0.0035
0.4	-0.2076	0.2668	0.0038
0.5	-0.2109	0.2726	0.0042
0.6	-0.2128	0.2761	0.0045
0.7	-0.2138	0.2782	0.0048
0.8	-0.2143	0.2794	0.0052
0.9	-0.2145	0.2800	0.0055
1.0	-0.2144	0.2803	0.0058

Appendix C.

C.1. Quadrupole Doublet, Hard-Edge

I(A)	Beam size (mm × mm)
0.27	1.7354×2.0775
0.28	1.60794×1.9589
0.29	1.4771×1.8357
0.3	1.3433×1.7081
0.31	1.2071×1.5760
0.32	1.0696×1.4394
0.33	0.9324×1.2984
0.34	0.7983×1.1531
0.35	0.6725×1.0035
0.36	0.5645×0.8499
0.37	0.4912×0.6926
0.38	0.4741×0.5325
0.39	0.5235×0.3720
0.40	0.6278×0.2209
0.41	0.7682×0.1398
0.42	0.9312×0.2356
0.43	1.1094×0.4021
0.44	1.2986×0.5858
0.45	1.4965×0.7779
0.46	1.7018×0.9762
0.47	1.9136×1.1799
0.48	2.1314×1.3887

Appendix D.

D.1. Quadrupole Doublet, Overall Transformation Matrix

D.1.1. Horizontal and Vertical Plane

I(A)	Beam size (mm × mm)
0.32	1.4584 × 1.8327
0.33	1.3367 × 1.7167
0.34	1.2133 × 1.5971
0.35	1.0888 × 1.4737
0.36	0.9644 × 1.3467
0.37	0.8422 × 1.2161
0.38	0.7254 × 1.0819
0.39	0.6199 × 0.9442
0.40	0.5356 × 0.8033
0.41	0.4874 × 0.6594
0.42	0.4898 × 0.5134
0.43	0.5456 × 0.3672
0.44	0.6439 × 0.2284
0.45	0.7711 × 0.1380
0.46	0.9174 × 0.1979
0.47	1.0768 × 0.3409
0.48	1.2460 × 0.5040
0.49	1.4229 × 0.6756
0.50	1.6064 × 0.8529
0.51	1.7956 × 1.0350
0.52	1.9901 × 1.2214

ϵ